

# Inclusive Production of $D^{*\pm}$ Mesons in Photon-Photon Collisions at $\sqrt{s_{ee}} = 183$ and $189$ GeV and a First Measurement of $F_{2,c}^\gamma$

The OPAL Collaboration

## Abstract

The inclusive production of  $D^{*\pm}$  mesons in photon-photon collisions has been measured using the OPAL detector at LEP at  $e^+e^-$  centre-of-mass energies  $\sqrt{s_{ee}}$  of 183 and 189 GeV. The  $D^{*+}$  mesons are reconstructed in their decay to  $D^0\pi^+$  with the  $D^0$  observed in the two decay modes  $K^-\pi^+$  and  $K^-\pi^+\pi^-\pi^+$ . After background subtraction,  $100.4 \pm 12.6$  (stat)  $D^{*\pm}$  mesons have been selected in events without observed scattered beam electron (“anti-tagged”) and  $29.8 \pm 5.9$  (stat)  $D^{*\pm}$  mesons in events where one beam electron is scattered into the detector (“single-tagged”). Direct and single-resolved events are studied separately. Differential cross-sections  $d\sigma/dp_T^{D^*}$  and  $d\sigma/d|\eta^{D^*}|$  as functions of the  $D^{*\pm}$  transverse momentum  $p_T^{D^*}$  and pseudorapidity  $\eta^{D^*}$  are presented in the kinematic region  $2 \text{ GeV} < p_T^{D^*} < 12 \text{ GeV}$  and  $|\eta^{D^*}| < 1.5$ . They are compared to next-to-leading order (NLO) perturbative QCD calculations. The total cross-section for the process  $e^+e^- \rightarrow e^+e^-c\bar{c}$  where the charm quarks are produced in the collision of two quasi-real photons is measured to be  $\sigma(e^+e^- \rightarrow e^+e^-c\bar{c}) = 842 \pm 97$  (stat)  $\pm 75$  (sys)  $\pm 196$  (extrapolation) pb. A first measurement of the charm structure function  $F_{2,c}^\gamma$  of the photon is performed in the kinematic range  $0.0014 < x < 0.87$  and  $5 \text{ GeV}^2 < Q^2 < 100 \text{ GeV}^2$ , and the result is compared to a NLO perturbative QCD calculation.

(To be submitted to Eur. Phys. J. C)

# The OPAL Collaboration

G. Abbiendi<sup>2</sup>, K. Ackerstaff<sup>8</sup>, P.F. Akesson<sup>3</sup>, G. Alexander<sup>23</sup>, J. Allison<sup>16</sup>, K.J. Anderson<sup>9</sup>,  
S. Arcelli<sup>17</sup>, S. Asai<sup>24</sup>, S.F. Ashby<sup>1</sup>, D. Axen<sup>29</sup>, G. Azuelos<sup>18,a</sup>, I. Bailey<sup>28</sup>, A.H. Ball<sup>8</sup>,  
E. Barberio<sup>8</sup>, T. Barillari<sup>2</sup>, R.J. Barlow<sup>16</sup>, J.R. Batley<sup>5</sup>, S. Baumann<sup>3</sup>, T. Behnke<sup>27</sup>, K.W. Bell<sup>20</sup>,  
G. Bella<sup>23</sup>, A. Bellerive<sup>9</sup>, S. Bentvelsen<sup>8</sup>, S. Bethke<sup>14,i</sup>, S. Betts<sup>15</sup>, O. Biebel<sup>14,i</sup>, A. Biguzzi<sup>5</sup>,  
I.J. Bloodworth<sup>1</sup>, P. Bock<sup>11</sup>, J. Böhme<sup>14,h</sup>, O. Boeriu<sup>10</sup>, D. Bonacorsi<sup>2</sup>, M. Boutemeur<sup>33</sup>,  
S. Braibant<sup>8</sup>, P. Bright-Thomas<sup>1</sup>, L. Brigliadori<sup>2</sup>, R.M. Brown<sup>20</sup>, H.J. Burckhart<sup>8</sup>,  
P. Capiluppi<sup>2</sup>, R.K. Carnegie<sup>6</sup>, A.A. Carter<sup>13</sup>, J.R. Carter<sup>5</sup>, C.Y. Chang<sup>17</sup>, D.G. Charlton<sup>1,b</sup>,  
D. Chrisman<sup>4</sup>, C. Ciocca<sup>2</sup>, P.E.L. Clarke<sup>15</sup>, E. Clay<sup>15</sup>, I. Cohen<sup>23</sup>, J.E. Conboy<sup>15</sup>, O.C. Cooke<sup>8</sup>,  
J. Couchman<sup>15</sup>, C. Couyoumtzelis<sup>13</sup>, R.L. Coxe<sup>9</sup>, M. Cuffiani<sup>2</sup>, S. Dado<sup>22</sup>, G.M. Dallavalle<sup>2</sup>,  
S. Dallison<sup>16</sup>, R. Davis<sup>30</sup>, A. de Roeck<sup>8</sup>, P. Dervan<sup>15</sup>, K. Desch<sup>27</sup>, B. Dienes<sup>32,h</sup>, M.S. Dixit<sup>7</sup>,  
M. Donkers<sup>6</sup>, J. Dubbert<sup>33</sup>, E. Duchovni<sup>26</sup>, G. Duckeck<sup>33</sup>, I.P. Duerdoth<sup>16</sup>, P.G. Estabrooks<sup>6</sup>,  
E. Etzion<sup>23</sup>, F. Fabbri<sup>2</sup>, A. Fanfani<sup>2</sup>, M. Fanti<sup>2</sup>, A.A. Faust<sup>30</sup>, L. Feld<sup>10</sup>, P. Ferrari<sup>12</sup>,  
F. Fiedler<sup>27</sup>, M. Fierro<sup>2</sup>, I. Fleck<sup>10</sup>, A. Frey<sup>8</sup>, A. Fürtjes<sup>8</sup>, D.I. Futyan<sup>16</sup>, P. Gagnon<sup>12</sup>,  
J.W. Gary<sup>4</sup>, G. Gaycken<sup>27</sup>, C. Geich-Gimbel<sup>3</sup>, G. Giacomelli<sup>2</sup>, P. Giacomelli<sup>2</sup>,  
D.M. Gingrich<sup>30,a</sup>, D. Glenzinski<sup>9</sup>, J. Goldberg<sup>22</sup>, W. Gorn<sup>4</sup>, C. Grandi<sup>2</sup>, K. Graham<sup>28</sup>,  
E. Gross<sup>26</sup>, J. Grunhaus<sup>23</sup>, M. Gruwé<sup>27</sup>, C. Hajdu<sup>31</sup>, G.G. Hanson<sup>12</sup>, M. Hansroul<sup>8</sup>, M. Hapke<sup>13</sup>,  
K. Harder<sup>27</sup>, A. Harel<sup>22</sup>, C.K. Hargrove<sup>7</sup>, M. Harin-Dirac<sup>4</sup>, M. Hauschild<sup>8</sup>, C.M. Hawkes<sup>1</sup>,  
R. Hawkings<sup>27</sup>, R.J. Hemingway<sup>6</sup>, G. Herten<sup>10</sup>, R.D. Heuer<sup>27</sup>, M.D. Hildreth<sup>8</sup>, J.C. Hill<sup>5</sup>,  
P.R. Hobson<sup>25</sup>, A. Hocker<sup>9</sup>, K. Hoffman<sup>8</sup>, R.J. Homer<sup>1</sup>, A.K. Honma<sup>8</sup>, D. Horváth<sup>31,c</sup>,  
K.R. Hossain<sup>30</sup>, R. Howard<sup>29</sup>, P. Hüntemeyer<sup>27</sup>, P. Igo-Kemenes<sup>11</sup>, D.C. Imrie<sup>25</sup>, K. Ishii<sup>24</sup>,  
F.R. Jacob<sup>20</sup>, A. Jawahery<sup>17</sup>, H. Jeremie<sup>18</sup>, M. Jimack<sup>1</sup>, C.R. Jones<sup>5</sup>, P. Jovanovic<sup>1</sup>, T.R. Junk<sup>6</sup>,  
N. Kanaya<sup>24</sup>, J. Kanzaki<sup>24</sup>, G. Karapetian<sup>18</sup>, D. Karlen<sup>6</sup>, V. Kartvelishvili<sup>16</sup>, K. Kawagoe<sup>24</sup>,  
T. Kawamoto<sup>24</sup>, P.I. Kayal<sup>30</sup>, R.K. Keeler<sup>28</sup>, R.G. Kellogg<sup>17</sup>, B.W. Kennedy<sup>20</sup>, D.H. Kim<sup>19</sup>,  
A. Klier<sup>26</sup>, T. Kobayashi<sup>24</sup>, M. Kobel<sup>3</sup>, T.P. Kokott<sup>3</sup>, M. Kolrep<sup>10</sup>, S. Komamiya<sup>24</sup>,  
R.V. Kowalewski<sup>28</sup>, T. Kress<sup>4</sup>, P. Krieger<sup>6</sup>, J. von Krogh<sup>11</sup>, T. Kuhl<sup>3</sup>, M. Kupper<sup>26</sup>, P. Kyberd<sup>13</sup>,  
G.D. Lafferty<sup>16</sup>, H. Landsman<sup>22</sup>, D. Lanske<sup>14</sup>, J. Lauber<sup>15</sup>, I. Lawson<sup>28</sup>, J.G. Layter<sup>4</sup>,  
D. Lellouch<sup>26</sup>, J. Letts<sup>12</sup>, L. Levinson<sup>26</sup>, R. Liebisch<sup>11</sup>, J. Lillich<sup>10</sup>, B. List<sup>8</sup>, C. Littlewood<sup>5</sup>,  
A.W. Lloyd<sup>1</sup>, S.L. Lloyd<sup>13</sup>, F.K. Loebinger<sup>16</sup>, G.D. Long<sup>28</sup>, M.J. Losty<sup>7</sup>, J. Lu<sup>29</sup>, J. Ludwig<sup>10</sup>,  
A. Macchiolo<sup>18</sup>, A. Macpherson<sup>30</sup>, W. Mader<sup>3</sup>, M. Mannelli<sup>8</sup>, S. Marcellini<sup>2</sup>, T.E. Marchant<sup>16</sup>,  
A.J. Martin<sup>13</sup>, J.P. Martin<sup>18</sup>, G. Martinez<sup>17</sup>, T. Mashimo<sup>24</sup>, P. Mättig<sup>26</sup>, W.J. McDonald<sup>30</sup>,  
J. McKenna<sup>29</sup>, E.A. Mckigney<sup>15</sup>, T.J. McMahon<sup>1</sup>, R.A. McPherson<sup>28</sup>, F. Meijers<sup>8</sup>,  
P. Mendez-Lorenzo<sup>33</sup>, F.S. Merritt<sup>9</sup>, H. Mes<sup>7</sup>, I. Meyer<sup>5</sup>, A. Micheli<sup>2</sup>, S. Mihara<sup>24</sup>,  
G. Mikenberg<sup>26</sup>, D.J. Miller<sup>15</sup>, W. Mohr<sup>10</sup>, A. Montanari<sup>2</sup>, T. Mori<sup>24</sup>, K. Nagai<sup>8</sup>, I. Nakamura<sup>24</sup>,  
H.A. Neal<sup>12,f</sup>, R. Nisius<sup>8</sup>, S.W. O’Neale<sup>1</sup>, F.G. Oakham<sup>7</sup>, F. Odorici<sup>2</sup>, H.O. Ogren<sup>12</sup>,  
A. Okpara<sup>11</sup>, M.J. Oreglia<sup>9</sup>, S. Orito<sup>24</sup>, G. Pásztor<sup>31</sup>, J.R. Pater<sup>16</sup>, G.N. Patrick<sup>20</sup>, J. Patt<sup>10</sup>,  
R. Perez-Ochoa<sup>8</sup>, S. Petzold<sup>27</sup>, P. Pfeifenschneider<sup>14</sup>, J.E. Pilcher<sup>9</sup>, J. Pinfold<sup>30</sup>, D.E. Plane<sup>8</sup>,  
B. Poli<sup>2</sup>, J. Polok<sup>8</sup>, M. Przybycień<sup>8,d</sup>, A. Quadt<sup>8</sup>, C. Rembser<sup>8</sup>, H. Rick<sup>8</sup>, S.A. Robins<sup>22</sup>,  
N. Rodning<sup>30</sup>, J.M. Roney<sup>28</sup>, S. Rosati<sup>3</sup>, K. Roscoe<sup>16</sup>, A.M. Rossi<sup>2</sup>, Y. Rozen<sup>22</sup>, K. Runge<sup>10</sup>,  
O. Runolfsson<sup>8</sup>, D.R. Rust<sup>12</sup>, K. Sachs<sup>10</sup>, T. Saeki<sup>24</sup>, O. Sahr<sup>33</sup>, W.M. Sang<sup>25</sup>,  
E.K.G. Sarkisyan<sup>23</sup>, C. Sbarra<sup>28</sup>, A.D. Schaile<sup>33</sup>, O. Schaile<sup>33</sup>, P. Scharff-Hansen<sup>8</sup>, J. Schieck<sup>11</sup>,  
S. Schmitt<sup>11</sup>, A. Schöning<sup>8</sup>, M. Schröder<sup>8</sup>, M. Schumacher<sup>3</sup>, C. Schwick<sup>8</sup>, W.G. Scott<sup>20</sup>,  
R. Seuster<sup>14,h</sup>, T.G. Shears<sup>8</sup>, B.C. Shen<sup>4</sup>, C.H. Shepherd-Themistocleous<sup>5</sup>, P. Sherwood<sup>15</sup>,  
G.P. Siroli<sup>2</sup>, A. Skuja<sup>17</sup>, A.M. Smith<sup>8</sup>, G.A. Snow<sup>17</sup>, R. Sobie<sup>28</sup>, S. Söldner-Rembold<sup>10,e</sup>,  
S. Spagnolo<sup>20</sup>, M. Sproston<sup>20</sup>, A. Stahl<sup>3</sup>, K. Stephens<sup>16</sup>, K. Stoll<sup>10</sup>, D. Strom<sup>19</sup>, R. Ströhmer<sup>33</sup>,  
B. Surrow<sup>8</sup>, S.D. Talbot<sup>1</sup>, P. Taras<sup>18</sup>, S. Tarem<sup>22</sup>, R. Teuscher<sup>9</sup>, M. Thiergen<sup>10</sup>, J. Thomas<sup>15</sup>,

M.A. Thomson<sup>8</sup>, E. Torrence<sup>8</sup>, S. Towers<sup>6</sup>, T. Trefzger<sup>33</sup>, I. Trigger<sup>18</sup>, Z. Trócsányi<sup>32,g</sup>,  
 E. Tsur<sup>23</sup>, M.F. Turner-Watson<sup>1</sup>, I. Ueda<sup>24</sup>, R. Van Kooten<sup>12</sup>, P. Vannerem<sup>10</sup>, M. Verzocchi<sup>8</sup>,  
 H. Voss<sup>3</sup>, F. Wäckerle<sup>10</sup>, D. Waller<sup>6</sup>, C.P. Ward<sup>5</sup>, D.R. Ward<sup>5</sup>, P.M. Watkins<sup>1</sup>, A.T. Watson<sup>1</sup>,  
 N.K. Watson<sup>1</sup>, P.S. Wells<sup>8</sup>, T. Wengler<sup>8</sup>, N. Wermes<sup>3</sup>, D. Wetterling<sup>11</sup>, J.S. White<sup>6</sup>,  
 G.W. Wilson<sup>16</sup>, J.A. Wilson<sup>1</sup>, T.R. Wyatt<sup>16</sup>, S. Yamashita<sup>24</sup>, V. Zacek<sup>18</sup>, D. Zer-Zion<sup>8</sup>

<sup>1</sup>School of Physics and Astronomy, University of Birmingham, Birmingham B15 2TT, UK

<sup>2</sup>Dipartimento di Fisica dell' Università di Bologna and INFN, I-40126 Bologna, Italy

<sup>3</sup>Physikalisches Institut, Universität Bonn, D-53115 Bonn, Germany

<sup>4</sup>Department of Physics, University of California, Riverside CA 92521, USA

<sup>5</sup>Cavendish Laboratory, Cambridge CB3 0HE, UK

<sup>6</sup>Ottawa-Carleton Institute for Physics, Department of Physics, Carleton University, Ottawa, Ontario K1S 5B6, Canada

<sup>7</sup>Centre for Research in Particle Physics, Carleton University, Ottawa, Ontario K1S 5B6, Canada

<sup>8</sup>CERN, European Organisation for Particle Physics, CH-1211 Geneva 23, Switzerland

<sup>9</sup>Enrico Fermi Institute and Department of Physics, University of Chicago, Chicago IL 60637, USA

<sup>10</sup>Fakultät für Physik, Albert-Ludwigs-Universität, D-79104 Freiburg, Germany

<sup>11</sup>Physikalisches Institut, Universität Heidelberg, D-69120 Heidelberg, Germany

<sup>12</sup>Indiana University, Department of Physics, Swain Hall West 117, Bloomington IN 47405, USA

<sup>13</sup>Queen Mary and Westfield College, University of London, London E1 4NS, UK

<sup>14</sup>Technische Hochschule Aachen, III Physikalisches Institut, Sommerfeldstrasse 26-28, D-52056 Aachen, Germany

<sup>15</sup>University College London, London WC1E 6BT, UK

<sup>16</sup>Department of Physics, Schuster Laboratory, The University, Manchester M13 9PL, UK

<sup>17</sup>Department of Physics, University of Maryland, College Park, MD 20742, USA

<sup>18</sup>Laboratoire de Physique Nucléaire, Université de Montréal, Montréal, Quebec H3C 3J7, Canada

<sup>19</sup>University of Oregon, Department of Physics, Eugene OR 97403, USA

<sup>20</sup>CLRC Rutherford Appleton Laboratory, Chilton, Didcot, Oxfordshire OX11 0QX, UK

<sup>22</sup>Department of Physics, Technion-Israel Institute of Technology, Haifa 32000, Israel

<sup>23</sup>Department of Physics and Astronomy, Tel Aviv University, Tel Aviv 69978, Israel

<sup>24</sup>International Centre for Elementary Particle Physics and Department of Physics, University of Tokyo, Tokyo 113-0033, and Kobe University, Kobe 657-8501, Japan

<sup>25</sup>Institute of Physical and Environmental Sciences, Brunel University, Uxbridge, Middlesex UB8 3PH, UK

<sup>26</sup>Particle Physics Department, Weizmann Institute of Science, Rehovot 76100, Israel

<sup>27</sup>Universität Hamburg/DESY, II Institut für Experimentalphysik, Notkestrasse 85, D-22607 Hamburg, Germany

<sup>28</sup>University of Victoria, Department of Physics, P O Box 3055, Victoria BC V8W 3P6, Canada

<sup>29</sup>University of British Columbia, Department of Physics, Vancouver BC V6T 1Z1, Canada

<sup>30</sup>University of Alberta, Department of Physics, Edmonton AB T6G 2J1, Canada

<sup>31</sup>Research Institute for Particle and Nuclear Physics, H-1525 Budapest, P O Box 49, Hungary

<sup>32</sup>Institute of Nuclear Research, H-4001 Debrecen, P O Box 51, Hungary

<sup>33</sup>Ludwigs-Maximilians-Universität München, Sektion Physik, Am Coulombwall 1, D-85748 Garching, Germany

<sup>a</sup> and at TRIUMF, Vancouver, Canada V6T 2A3

<sup>b</sup> and Royal Society University Research Fellow

<sup>c</sup> and Institute of Nuclear Research, Debrecen, Hungary

<sup>d</sup> and University of Mining and Metallurgy, Cracow

<sup>e</sup> and Heisenberg Fellow

<sup>f</sup> now at Yale University, Dept of Physics, New Haven, USA

<sup>g</sup> and Department of Experimental Physics, Lajos Kossuth University, Debrecen, Hungary

<sup>h</sup> and MPI München

<sup>i</sup> now at MPI für Physik, 80805 München.

## 1 Introduction

Charged  $D^*$  mesons<sup>1</sup> provide a clean tag to study open charm production in photon-photon collisions. The inclusive cross-section for the production of  $D^*$  mesons can be calculated in perturbative QCD (pQCD). Since the process is characterised by two distinct scales, the mass  $m_c$  and the transverse momentum  $p_T$  of the charm quarks, two different approaches exist for the next-to-leading order (NLO) pQCD calculations. In the “massless” scheme, charm is treated as an active flavour in the photon. This approach is expected to be valid for  $p_T \gg m_c$ . In the “massive” scheme, matrix elements for massive charm quarks are used and no charm content is assigned to the parton distributions of the photon. One expects this ansatz to be valid at  $p_T \approx m_c$  [1].

A third scale is the four-momentum squared,  $Q_{i=1,2}^2$ , of the interacting virtual photons. In this paper, two kinematic cases are studied, depending on  $Q_i^2$ . For the largest part of the cross-section, both exchanged photons are quasi-real ( $Q_1^2, Q_2^2 \approx 0$ ) and the beam electrons are scattered at very small angles. These events are selected by rejecting events with a scattered electron in the detector. Events of this type are called anti-tagged. If a photon is highly virtual ( $Q_i^2 \gg 0$ ), the corresponding beam electron is usually scattered into the acceptance of the detector. Events with one detected scattered electron are called single-tagged.

In direct events, the two photons couple directly to the  $c\bar{c}$  pair. In resolved events, one photon (“single-resolved”) or both photons (“double-resolved”) fluctuate into a hadronic state and a gluon or a quark of the hadronic fluctuation of the photon takes part in the hard interaction. For anti-tagged events at  $e^+e^-$  centre-of-mass energies  $\sqrt{s_{ee}}$  around 189 GeV, the production of  $D^*$  mesons in photon-photon collisions in leading order (LO) QCD proceeds mainly via direct ( $\gamma\gamma \rightarrow c\bar{c}$ ) and single-resolved ( $g\gamma \rightarrow c\bar{c}$ ) photon-photon processes [2, 3], whereas the contribution from double-resolved events ( $gg \rightarrow c\bar{c}$ ) is expected to be small. The measurement of the open charm cross-section is therefore expected to be sensitive to the gluon content of the photon through the photon-gluon fusion process  $g\gamma \rightarrow c\bar{c}$ . The production of  $D^*$  mesons from open bottom production in photon-photon events is expected to be suppressed by more than

---

<sup>1</sup>Throughout this paper  $D^*$  refers to  $D^{*+}$  as well as to  $D^{*-}$ . Charge conjugated modes are always implied.

two orders of magnitude [2]. Bottom production is suppressed due to the smaller electric charge and the larger mass of the b quarks.

The single-tagged process can be regarded as deep inelastic electron-photon scattering. In this configuration, the electron radiating the highly virtual photon,  $\gamma^*$ , probes the structure of the quasi-real photon,  $\gamma$ , radiated from the second beam electron, and allows the determination of the photon structure function  $F_2^\gamma(x, Q^2)$ . Here  $x$  is the Bjorken scaling variable and  $Q^2$  the virtuality of the highly virtual photon. Due to the large mass of the charm quark, the charm structure function  $F_{2,c}^\gamma$  of the photon can be calculated in pQCD to NLO [4]. In QCD,  $F_{2,c}^\gamma$  receives contributions from the point-like and the hadron-like structure of the quasi-real photon. The two contributions are expected to be well separated in  $x$ , with the point-like contribution dominating at high  $x$  and the hadron-like component sizeable only for  $x < 0.1$ .

The production of  $D^*$  mesons in photon-photon events has been measured previously by JADE [5], TASSO [6], TPC/2 $\gamma$  [7], TOPAZ [8], AMY [9], ALEPH [10] and L3 [11] at  $\sqrt{s_{ee}}$  ranging from 29 GeV up to 189 GeV. The charm structure function  $F_{2,c}^\gamma$  of the photon has never been measured before. The analysis presented here uses the data taken with the OPAL detector in 1997 at  $\sqrt{s_{ee}} = 183$  GeV and in 1998 at  $\sqrt{s_{ee}} = 189$  GeV with integrated luminosities  $\mathcal{L}$  of 55 and 165  $\text{pb}^{-1}$ , respectively.

## 2 The OPAL detector

A detailed description of the OPAL detector can be found in Ref. [12], and therefore only a brief account of the main features relevant to the present analysis will be given here.

The central tracking system is located inside a solenoidal magnet which provides a uniform axial magnetic field of 0.435 T along the beam axis<sup>2</sup>. The magnet is surrounded by a lead-glass electromagnetic calorimeter (ECAL) and a hadronic sampling calorimeter (HCAL). Outside the HCAL, the detector is surrounded by muon chambers. There are similar layers of detectors in the endcaps. The region around the beam pipe on both sides of the detector is covered by the forward calorimeters and the silicon-tungsten luminometers.

Starting with the innermost components, the tracking system consists of a high precision silicon microvertex detector (SI), a precision vertex drift chamber (CV), a large volume jet chamber (CJ) with 159 layers of axial anode wires and a set of  $z$  chambers measuring the track coordinates along the beam direction. The transverse momenta  $p_T$  of tracks are measured with a precision of  $\sigma_{p_T}/p_T = \sqrt{0.02^2 + (0.0015 \cdot p_T)^2}$  ( $p_T$  in GeV)<sup>3</sup> in the central region  $|\cos \theta| < 0.73$ . In this paper, transverse is always defined with respect to the  $z$  direction of the detector. The jet chamber also provides energy loss measurements which are used for particle identification.

The ECAL completely covers the azimuthal range for polar angles satisfying  $|\cos \theta| < 0.98$ . The barrel section, which covers the polar angle range  $|\cos \theta| < 0.82$ , consists of a cylindrical

---

<sup>2</sup>In the OPAL coordinate system the  $x$  axis points towards the centre of the LEP ring, the  $y$  axis points upwards and the  $z$  axis points in the direction of the electron beam. The polar angle  $\theta$  is defined with respect to the  $z$  axis.

<sup>3</sup>Throughout this paper we use the convention  $c = 1$ .

array of 9440 lead-glass blocks with a depth of 24.6 radiation lengths. The endcap sections consist of 1132 lead-glass blocks with a depth of more than 22 radiation lengths, covering the polar angle between  $0.81 < |\cos \theta| < 0.98$ .

The forward calorimeters (FD) at each end of the OPAL detector consist of cylindrical lead-scintillator calorimeters with a depth of 24 radiation lengths divided azimuthally into 16 segments. The electromagnetic energy resolution is about  $18\%/\sqrt{E}$  ( $E$  in GeV). The acceptance of the forward calorimeters covers the angular range from 47 to 140 mrad from the beam direction. Three planes of proportional tube chambers at 4 radiation lengths depth in the calorimeter measure the directions of electron showers with a precision of approximately 1 mrad.

The silicon tungsten detectors (SW) [13] at each end of the OPAL detector cover an angular region between 33 and 59 mrad in front of the forward calorimeters. Each calorimeter consists of 19 layers of silicon detectors and 18 layers of tungsten, corresponding to a total of 22 radiation lengths. Each silicon layer consists of 16 wedge-shaped silicon detectors. The electromagnetic energy resolution is about  $25\%/\sqrt{E}$  ( $E$  in GeV). The radial position of electron showers in the SW calorimeter can be determined with a typical resolution of 0.06 mrad in the polar angle  $\theta$ .

### 3 Process kinematics

The kinematic properties of the two interacting photons are described by their negative squared four-momentum transfers,  $Q_{i=1,2}^2$ , which are related to the scattering angles  $\theta'_i$  relative to the beam direction of the corresponding electrons by

$$Q_i^2 = -(k_i - k'_i)^2 \approx 2E_i E'_i (1 - \cos \theta'_i), \quad (1)$$

neglecting the mass  $m_e$  of the electron. The quantities  $k_i$  and  $k'_i$  are the four-momenta of the beam and scattered electrons, and  $E_i$  and  $E'_i$  are their respective energies. The flux of transversely polarized quasi-real photons with an energy fraction  $z$  of the beam energy and a negative squared four-momentum, denoted with  $Q_i^2$ , may be obtained by the Equivalent Photon Approximation (EPA) [14]:

$$\frac{d^2 N_\gamma}{dz dQ_i^2} = \frac{\alpha}{2\pi} \left( \frac{1 + (1-z)^2}{z Q_i^2} - \frac{2m_e^2 z}{Q_i^4} \right), \quad (2)$$

where  $\alpha$  is the fine structure constant. The minimum kinematically allowed squared four-momentum transfer,  $Q_{\min}^2$ , is determined by the electron mass,

$$Q_{\min}^2 = \frac{m_e^2 z^2}{1-z}. \quad (3)$$

The maximum squared four-momentum transfer,  $Q_{\max}^2$ , is given by the experimental anti-tagging condition according to Eq. 1.

If one of the photons is highly virtual ( $Q_1^2 \equiv Q^2 = -q^2 \gg Q_2^2 \equiv P^2 = -p^2 \approx 0$ ), the cross-section of the process  $e^+e^- \rightarrow e^+e^-c\bar{c}$  can be written as a product of the deep inelastic electron-photon scattering cross-section and the flux of quasi-real photons,

$$\frac{d^4 \sigma_{e^+e^- \rightarrow e^+e^-c\bar{c}}}{dx dQ^2 dz dP^2} = \frac{d^2 \sigma_{e\gamma \rightarrow ec\bar{c}}}{dx dQ^2} \cdot \frac{d^2 N_\gamma}{dz dP^2}. \quad (4)$$

The differential deep inelastic electron-photon scattering cross-section may be parametrised in terms of structure functions as [15]

$$\frac{d^2\sigma_{e\gamma\rightarrow ec\bar{c}}}{dx dQ^2} = \frac{2\pi\alpha^2}{xQ^4} \cdot \left[ (1 + (1-y)^2)F_{2,c}^\gamma(x, Q^2) - y^2 F_{L,c}^\gamma(x, Q^2) \right], \quad (5)$$

where  $x = Q^2/2pq$  and the inelasticity  $y = pq/pk_1$  are the usual dimensionless deep inelastic scattering variables. In the kinematic regime studied in this paper,  $y^2 \ll 1$ . The contribution proportional to  $F_{L,c}^\gamma(x, Q^2)$  in Eq. 5 is therefore neglected. The variable  $x$  is experimentally accessible via the relation

$$x = \frac{Q^2}{Q^2 + W^2 + P^2} \approx \frac{Q^2}{Q^2 + W^2}, \quad (6)$$

where  $W^2$  is the invariant mass squared of the photon-photon system. The event selection ensures that the virtuality  $P^2$  is usually very small compared to  $Q^2$ , so  $P^2$  is neglected for the determination of  $x$  from Eq. 6. By measuring the deep inelastic electron-photon scattering cross-section for  $e^+e^- \rightarrow e^+e^-c\bar{c}$  as a function of  $x$  and  $Q^2$ , the charm structure function  $F_{2,c}^\gamma(x, Q^2)$  of the photon can be determined.

## 4 Monte Carlo simulation

For real photons the PYTHIA 6.121 [16] photon-photon Monte Carlo program, based on LO pQCD calculations, is used to simulate the process  $e^+e^- \rightarrow e^+e^-\gamma\gamma \rightarrow e^+e^-c\bar{c} \rightarrow e^+e^-D^*X$  ( $X$  is a hadronic system). Two distinct samples, one for the direct process,  $\gamma\gamma \rightarrow c\bar{c}$ , and one for the single-resolved process,  $g\gamma \rightarrow c\bar{c}$ , were generated using matrix elements for massive charm quarks. The different  $e^+e^-$  centre-of-mass energies,  $\sqrt{s_{ee}} = 183$  and 189 GeV, are taken into account by generating events at both energies according to the ratio of the corresponding integrated luminosities. In case of the single-resolved process, the SaS-1D parametrisation [17] is used for the parton distributions of the photon. The fragmentation of the charm quarks is modelled using the Peterson fragmentation function [18] with the PYTHIA default parameter  $\epsilon_c = 0.031$ , and the charm mass is set to  $m_c = 1.6$  GeV. The resulting average scaled energy of the generated  $D^*$  mesons is  $\langle x_{D^*} \rangle = 2 \cdot \langle E_{D^*}/W \rangle = 0.84$ , where  $E_{D^*}$  is the  $D^*$  energy in the photon-photon centre-of-mass system. Final state QCD radiation off the primary charm quarks is taken into account using the leading-log approximation. A sample of double-resolved quasi-real photon-photon events ( $gg \rightarrow c\bar{c}$ ) was also generated with the PYTHIA 6.121 Monte Carlo generator.

The LO Monte Carlo generators HERWIG 5.9 [19] and Vermaseren [20] are used to model the  $D^*$  production in deep inelastic electron-photon scattering,  $e^+e^- \rightarrow e^+e^-\gamma^*\gamma \rightarrow e^+e^-c\bar{c} \rightarrow e^+e^-D^*X$ . For both Monte Carlo generators, the charm quark mass is chosen to be  $m_c = 1.5$  GeV. In HERWIG, the cross-section is evaluated for massless charm quarks. The charm production is modelled using matrix elements for massless charm quarks, together with the GRV parametrisation [21] for the parton distributions of the photon, again for massless charm quarks. The effect of the charm quark mass is accounted for rather crudely by not simulating events with  $W < 2m_c$ , giving an unphysically sharp step in the cross-section at this threshold. Due to the massless approach used in HERWIG and the crude treatment at threshold, the predicted

charm production cross-section is likely to be too large. Nevertheless, the final state kinematics are treated correctly, so HERWIG can be used for the determination of selection efficiencies. The fragmentation of quarks into hadrons is modelled via the cluster fragmentation model yielding an average scaled energy of the generated  $D^*$  mesons of  $\langle x_{D^*} \rangle = 0.64$ . The Vermaseren generator is based on the Quark Parton Model (QPM) and consequently does not take into account the hadron-like component of the photon structure. It models the complete dependence of the cross-section on the different photon helicities. The fragmentation into hadrons is handled via JETSET 7.4 [16], where the same fragmentation model is used as for the PYTHIA Monte Carlo described above. The average scaled energy of the generated  $D^*$  mesons is  $\langle x_{D^*} \rangle = 0.82$ , close to the PYTHIA value.

The  $e^+e^-$  annihilation background with  $D^*$  mesons in the final state has been simulated with the PYTHIA 5.7 Monte Carlo model. The Monte Carlo generator GRC4F [22] was used to simulate four-fermion processes that are background to the photon-photon sample. All Monte Carlo samples were generated with full simulation of the OPAL detector [23]. They are analysed using the same reconstruction algorithms as applied to the data.

## 5 Event selection and $D^*$ reconstruction

In this and in the following three sections, only anti-tagged photon-photon scattering events are studied; the analysis of tagged electron-photon scattering events is described in section 9. Because the difference of the  $e^+e^-$  centre-of-mass energies of  $\sqrt{s}_{ee} = 183$  and 189 GeV is small the data samples recorded at both energies are combined. Anti-tagged photon-photon events are selected using the following set of cuts:

- At least three tracks must have been found in the tracking chambers (SI, CV and CJ). A track is required to have a minimum transverse momentum of 120 MeV, more than 20 hits in the central jet chamber used to calculate the specific energy loss  $dE/dx$ , and the innermost hit of the track must be inside a radius of 60 cm with respect to the  $z$  axis. The distance of closest approach to the origin must be less than 20 cm in the  $z$  direction and less than 1 cm in the  $r\phi$  plane.
- To reduce background from  $e^+e^-$  annihilation events with  $D^*$  mesons in the final state, the sum of all energy deposits in the ECAL is required to be less than 40 GeV. Calorimeter clusters have to pass an energy threshold of 100 MeV for the barrel section and 250 MeV for the endcap sections.
- To reduce the  $e^+e^-$  annihilation background further, the visible invariant mass of the event,  $W_{\text{vis}}$ , should be less than 60 GeV.  $W_{\text{vis}}$  is calculated using the energies and positions of clusters measured in the ECAL, the HCAL, the FD and the SW calorimeters and using the momenta of tracks. A matching algorithm [24] is applied to avoid double-counting of particle momenta in the calorimeters and in the tracking chambers.
- Anti-tagged events are selected by vetoing all events containing an energy deposit of more than 50 GeV in the SW or FD in either hemisphere of the detector. This corresponds to a maximum allowed scattering angle of the beam electrons of  $\theta' = 33$  mrad for electrons with  $E' > 50$  GeV.



The method of reconstructing  $D^*$  mesons is similar to that used in former OPAL analyses [25]. It exploits the small mass difference between the  $D^*$  and the  $D^0$  mesons which causes the kinetic energy of the slow pion in the decay  $D^{*+} \rightarrow D^0 \pi^+$  to be only 6 MeV in the  $D^*$  rest frame. Thus, the combinatorial background is small due to the limited phase space. The  $D^0$  mesons are identified via their decay  $D^0 \rightarrow K^- \pi^+$  and  $D^0 \rightarrow K^- \pi^+ \pi^- \pi^+$ , which form, together with the slow pion, the “3-prong” and “5-prong” decay modes of the  $D^*$ , respectively.

In the 3-prong decay mode, all combinations of two oppositely charged tracks in an event are used to form  $D^0$  candidates. The  $dE/dx$  probability  $\mathcal{P}_K^{dE/dx}$  for the kaon hypothesis should exceed 10% for at least one of the two tracks. The invariant mass  $M_{D^0}^{\text{cand}}$  of this combination is calculated, assigning the kaon mass to the kaon candidate and the pion mass to the other track. If for both tracks  $\mathcal{P}_K^{dE/dx}$  is greater than 10%, both possible  $K\pi$  combinations are used.

If  $M_{D^0}^{\text{cand}}$  lies within a window around the nominal  $D^0$  mass,

$$1790 \text{ MeV} < M_{D^0}^{\text{cand}} < 1940 \text{ MeV}, \quad (7)$$

the combination is retained as a  $D^0$  candidate. All remaining tracks of opposite charge to the kaon candidate are then examined and the invariant mass  $M_{D^*}^{\text{cand}}$  of the  $D^*$  candidates is calculated assigning the pion mass to the third track.

Random combinations of low-momentum tracks are the largest source of background passing the above cuts. To reduce this background, we exploit the fact that the  $D^0$  is a pseudo-scalar particle which decays isotropically in its rest frame. This leads to a flat distribution of  $\cos \theta^*$ , where  $\theta^*$  denotes the decay angle between the direction of the kaon in the  $D^0$  rest frame and the direction of the  $D^0$  in the laboratory frame. In contrast, background events exhibit a pronounced peak at  $\cos \theta^* = 1$ . Therefore we require  $\cos \theta^* < 0.9$ .

In the 5-prong decay mode, the procedure is similar but, due to higher combinatorial background, some cuts are tightened. To form the  $D^0$  candidate, four tracks are combined if the charges of the tracks add up to zero. One track should be identified as a kaon, i.e.  $\mathcal{P}_K^{dE/dx} > 10\%$ , and this track’s  $dE/dx$  probability  $\mathcal{P}_\pi^{dE/dx}$  for the pion hypothesis should be less than 10%. For the other three tracks,  $\mathcal{P}_\pi^{dE/dx}$  is required to be larger than 0.5%. If the mass of the  $D^0$  candidate lies in the range

$$1830 \text{ MeV} < M_{D^0}^{\text{cand}} < 1900 \text{ MeV}, \quad (8)$$

a fifth track is added, with  $\mathcal{P}_\pi^{dE/dx} > 0.5\%$  and a charge opposite to the charge of the kaon candidate, to form the  $D^*$  candidate.

To further reduce the combinatorial background in both decay modes, a minimum transverse momentum  $p_T^{D^*}$  of the  $D^*$  of 2 GeV is required. To ensure that the tracks forming the  $D^*$  candidates are mostly contained in the tracking chambers, the pseudorapidity  $\eta^{D^*}$  of the  $D^*$  is required to be within  $|\eta^{D^*}| < 1.5$ , with  $\eta^{D^*} = -\ln \tan(\theta/2)$ . The angle  $\theta$  is the polar angle of the  $D^*$  candidate.

In about 30% (8%) of the events with 5-prong (3-prong) candidates, more than one  $D^*$  candidate passes the above cuts on  $p_T^{D^*}$  and  $\eta^{D^*}$ . Since the probability to correctly reconstruct two different  $D^*$  mesons in one event is negligibly small, only the  $D^*$  candidates with  $M_{D^0}^{\text{cand}}$  closest to the  $D^0$  mass of 1864.6 MeV [26] are retained in events with more than one  $D^*$

candidate. It has been checked that this method does not produce any biases. In approximately 6% of the events, two or more  $D^*$  candidates in an event share the same  $D^0$  candidate, but different tracks were assigned as slow-pion candidate. All of these  $D^*$  candidates are kept.

Fig. 1 shows the difference between the  $D^*$  and the  $D^0$  candidate mass for both decay channels for events with  $\Delta M \equiv M_{D^*}^{\text{cand}} - M_{D^0}^{\text{cand}} < 200.5$  MeV. A clear peak is observed around  $\Delta M = 145.4$  MeV which is the mass difference between the  $D^*$  and the  $D^0$  meson [26]. A fit of a background function,

$$f(\Delta M) = a \cdot (\Delta M - m_\pi)^b, \quad (9)$$

is performed to the upper sideband of the signal, defined by  $160.5 \text{ MeV} < \Delta M < 200.5 \text{ MeV}$ , where  $m_\pi$  is the pion mass and  $a$  and  $b$  are free parameters. The  $\chi^2$  of the fit is 13 for 18 degrees of freedom. The fit result is superimposed for the whole  $\Delta M$  range. In the signal region, defined as  $142.5 \text{ MeV} < \Delta M < 148.5 \text{ MeV}$ , a number of  $100.4 \pm 12.6$  (stat)  $D^*$  mesons is obtained after subtracting the fitted background from the total number of events in the signal region. The distribution of the wrong-charge background is also shown. It is obtained from the data applying identical cuts as for the signal, but requiring that the charges of the tracks forming the  $D^0$  candidate should add up to  $-2$  instead of  $0$ . In addition, in the 5-prong mode the three pion tracks should not have equal charges. In the upper sideband, the wrong-charge sample gives a good description of the shape and normalisation of the background in the signal sample. Hence, no normalisation is applied to the wrong-charge sample.

Using the Monte Carlo simulations,  $D^*$  mesons produced in  $e^+e^-$  annihilation events are found to contribute only around 1% to the  $D^*$  signal. It was checked that the  $e^+e^-$  background is negligible for all values of  $p_T^{D^*}$ . Non-photon-photon four-fermion background is also found to be negligible.

## 6 Separation of direct and single-resolved events

We use two different methods to study the relative contributions of the direct and single-resolved processes to the data sample. First, we study di-jet events using the method described in more detail in Ref. [27]. In di-jet events, two experimental variables can be defined,  $x_\gamma^+$  and  $x_\gamma^-$ , which are measures of the photon momenta participating in the hard interaction. They are calculated using the relation

$$x_\gamma^\pm = \frac{\Sigma_{\text{jets}}(E \pm p_z)}{\Sigma_{\text{hadrons}}(E \pm p_z)}, \quad (10)$$

where  $p_z$  is the momentum component along the  $z$  axis of the detector and  $E$  is the energy of the jets or hadrons, respectively. Assuming in the LO picture that the two jets contain all the decay products of the two charm quarks, we expect for direct events that the whole energy of the event is contained in the two jets, i.e.  $x_\gamma^+$  and  $x_\gamma^-$  are close to 1. In resolved events, there is also energy outside the two jet cones due to the photon remnant(s). Events where either  $x_\gamma^+$  or  $x_\gamma^-$  is much smaller than 1 are expected to originate from single-resolved processes. Events where both  $x_\gamma^+$  and  $x_\gamma^-$  are much smaller than 1 are expected to originate from double-resolved processes. The validity of this expectation has been demonstrated in Ref. [27].

The second method can be used for all  $D^*$  event, not just the di-jet sub-sample. We can

reconstruct the scaled  $D^*$  transverse momentum  $x_T^{D^*}$  which is given by

$$x_T^{D^*} = \frac{2p_T^{D^*}}{W_{\text{vis}}}. \quad (11)$$

If  $p_T^{D^*}$  is a good estimate of the transverse momentum of the charm quarks and if the charm quarks are produced centrally ( $\eta = 0$ ), the variable  $x_T^{D^*}$  is equal to  $x_\gamma^\pm$ . This variable is therefore sensitive to the ratio of the direct and the single-resolved process. As in the case of the  $x_\gamma^\pm$  distribution, the direct contribution dominates at high values of  $x_T^{D^*}$ , whereas the single-resolved events are concentrated at small  $x_T^{D^*}$ , as predicted by the Monte Carlo.

In order to reconstruct jets, a cone jet finding algorithm is applied to the signal events. As in the calculation of  $W_{\text{vis}}$ , the energy and positions of all clusters in the ECAL, the HCAL, the FD and the SW calorimeters and the momenta of all tracks are used in the jet finding after applying the matching algorithm [24] to avoid double counting of particle momenta. The cone size  $R = \sqrt{(\Delta\eta)^2 + (\Delta\phi)^2}$  is set equal to 1, where  $\eta$  and  $\phi$  denote the pseudorapidity and the azimuthal angle, respectively. The minimum transverse jet energy  $E_T^{\text{jet}}$  is required to be greater than 3 GeV. The pseudorapidity of the reconstructed jets must be less than 2.

In Fig. 2, the fraction of events with different number of jets,  $n^{\text{jet}}$ , is shown for events in the signal region for data and for the direct and the single-resolved PYTHIA Monte Carlo samples, separately. About 1/3 of the data events are di-jet events. The number of signal events in the direct (single-resolved) Monte Carlo sample is approximately 6.5 (3.5) times the number of signal events in the data. In the data, the combinatorial background has been subtracted using the  $n^{\text{jet}}$  distribution from the upper  $\Delta M$  sideband. The agreement between the  $n^{\text{jet}}$  distributions in the data and the Monte Carlo is satisfactory. There are slightly more data events in the 3-jet bin and less data events in the 2-jet bin compared to PYTHIA. Only a small difference between the number of jets found in direct and single-resolved events is expected according to the Monte Carlo.

Fig. 3 shows the distribution of  $x_\gamma^{\text{min}} = \min(x_\gamma^+, x_\gamma^-)$ . In the data, the combinatorial background has been subtracted using events from the  $\Delta M$  sideband. At small values of  $x_\gamma^{\text{min}}$ , the distribution is approximately flat, but for large  $x_\gamma^{\text{min}}$  values a clear enhancement is visible. This is expected to be due to the direct process. The PYTHIA Monte Carlo predicts 87% of the direct di-jet events to have  $x_\gamma^{\text{min}} > 0.7$  and 82% of the single-resolved di-jet events to have  $x_\gamma^{\text{min}} < 0.7$ .

The ratio of direct to single-resolved contributions in the di-jet data is determined by a fit to the  $x_\gamma^{\text{min}}$  distribution using the method of least squares ( $\chi^2$  fit). In the fit, the sum of the direct and single-resolved Monte Carlo samples is fixed to the number of di-jet events in the data, but the ratio of direct to single-resolved events is left free. According to the PYTHIA Monte Carlo, a significant contribution of double-resolved events in the data should show up as a clear enhancement at small  $x_\gamma^{\text{min}}$  values. As expected from Ref. [2], this is not observed, and the contribution from double-resolved events is therefore neglected. The fit yields that  $(46 \pm 11)\%$  of the di-jet events in the data are due to the direct and  $(54 \pm 11)\%$  are due to the single-resolved process. In Fig. 3, the fitted direct and single-resolved contributions are shown. The  $\chi^2$  of the fit result is 6.1 for 9 degrees of freedom, and the fit result gives a good description of the data. At high  $x_\gamma^{\text{min}}$  values, where the direct events are concentrated, the data seem to be slightly shifted towards smaller  $x_\gamma^{\text{min}}$  values compared to the Monte Carlo.

In Fig. 4, the scaled  $D^*$  transverse momentum  $x_T^{D^*}$  is plotted for all signal events after subtracting the combinatorial background. The ratio of direct to single-resolved contributions in the data is again determined by a fit using the same procedure as applied to the  $x_\gamma^{\min}$  distribution. Poisson errors are assigned to the bins without data entry. The fit yields that  $(51 \pm 9)\%$  of the signal events in the data are due to the direct and  $(49 \pm 9)\%$  are due to the single-resolved process, consistent with the result of the fit to the  $x_\gamma^{\min}$  distribution. In Fig. 4 the fitted direct and single-resolved contributions are shown. The  $\chi^2$  of the fit result is 6.5 for 13 degrees of freedom. Again, the fit result gives a good description of the data.

Since in the fit to the  $x_T^{D^*}$  distribution all signal events are used, whereas in case of the  $x_\gamma^{\min}$  distribution the fit is applied only to a part of the signal events, we use the result of the fit to the  $x_T^{D^*}$  distribution in the further analysis.

Table 1 summarises the  $D^*$  selection efficiencies  $\epsilon$  for the 3-prong and the 5-prong decay modes in direct and single-resolved events. The efficiencies are calculated using the Monte Carlo by dividing the number of reconstructed  $D^*$  mesons by the number of generated  $D^*$  mesons with  $p_T^{D^*} > 2$  GeV and  $|\eta^{D^*}| < 1.5$ . In the 5-prong mode, the selection efficiency for direct events is slightly higher than for single-resolved events, whereas in the 3-prong mode the selection efficiencies are about equal for direct and single-resolved event. The fractions of direct and single-resolved  $e^+e^- \rightarrow e^+e^-D^*X$  events in the kinematical region  $p_T^{D^*} > 2$  GeV and  $|\eta^{D^*}| < 1.5$  are therefore assumed to be unchanged by the efficiency correction. To determine the systematic uncertainty, half the difference between the direct and single-resolved efficiencies in the 5-prong mode is used and no systematic uncertainty is used for the 3-prong mode. Together with the relative rate of  $D^*$  mesons decaying in the 5-prong mode and the 3-prong mode, this yields a 8% relative uncertainty which is added quadratically to the 18% relative error of the direct and single-resolved contributions determined by the fit to the  $x_T^{D^*}$  distribution. The direct contribution of the process  $e^+e^- \rightarrow e^+e^-D^*X$  in the kinematical region  $p_T^{D^*} > 2$  GeV and  $|\eta^{D^*}| < 1.5$  is determined to be  $r_{\text{dir}} = (51 \pm 10)\%$  and the single-resolved process contributes to a fraction of  $1 - r_{\text{dir}} = (49 \pm 10)\%$ . No significant double-resolved contribution is observed.

## 7 Differential $D^*$ cross-sections

We determine the differential cross-sections  $d\sigma/dp_T^{D^*}$  and  $d\sigma/d|\eta^{D^*}|$  for the production of  $D^*$  mesons in anti-tagged  $e^+e^- \rightarrow e^+e^-D^*X$  events as a function of the transverse momentum  $p_T^{D^*}$  and the pseudorapidity  $|\eta^{D^*}|$ . Table 2 summarises the background-subtracted number  $N_{D^*}^{\text{rec}}$  of  $D^*$  mesons and the differential cross-section  $d\sigma/dp_T^{D^*}$  for both decay modes. At large  $p_T^{D^*}$  the statistical errors are large for the upper  $\Delta M$  sidebands of the signal and for the wrong-charge distributions. These two distributions are therefore combined to determine the background in each decay mode and  $p_T^{D^*}$  bin. The background function  $f(\Delta M) = a \cdot (\Delta M - m_\pi)^b$  is fitted to this upper sideband distribution and the number of background events is calculated from the fit result.

For each decay mode and for each bin in  $p_T^{D^*}$ , the differential cross-section  $d\sigma/dp_T^{D^*}$  is calculated using the relation

$$\frac{d\sigma}{dp_T^{D^*}} = \frac{N_{D^*}^{\text{rec}}}{\epsilon \cdot \text{BR} \cdot \mathcal{L} \cdot \Delta p_T^{D^*}}. \quad (12)$$

The efficiency  $\epsilon$  is determined using the Monte Carlo by fixing the ratio of direct to single-resolved events to the result obtained in the previous section. The branching ratios  $\text{BR}(D^{*+} \rightarrow K^- \pi^+ \pi^+) = 0.02630 \pm 0.00082$  and  $\text{BR}(D^{*+} \rightarrow K^- \pi^+ \pi^- \pi^+ \pi^+) = 0.0519 \pm 0.0029$  are taken from Ref. [26],  $\mathcal{L}$  is the total integrated luminosity and  $\Delta p_T^{D^*}$  is the width of the  $p_T^{D^*}$  bin. The results of both decay modes agree within the statistical uncertainties. The combined differential cross-section  $d\sigma/dp_T^{D^*}$  is given in Table 2. The average transverse momentum  $\langle p_T^{D^*} \rangle$  for each bin is determined using the method proposed in Ref. [28].

In Fig. 5, the combined differential cross-section  $d\sigma/dp_T^{D^*}$  is compared to the NLO calculation by Frixione et al. [3] using the massive approach and to the NLO calculation by Kniehl et al. [29] using the massless approach, which was repeated by the authors specifically for the kinematical conditions of this analysis. In both calculations, the charm quark mass is taken to be  $m_c = 1.5$  GeV and the charm fragmentation is parametrised by the Peterson fragmentation function. The Peterson fragmentation parameter  $\epsilon_c$  and the fraction  $f(c \rightarrow D^{*+})$  of charm quarks fragmenting into  $D^{*+}$  meson are  $\epsilon_c = 0.116$ ,  $f(c \rightarrow D^{*+}) = 0.267$  in the massless calculation and  $\epsilon_c = 0.035$ ,  $f(c \rightarrow D^{*+}) = 0.233$  in the massive calculation. For the massless calculation, the parameters were determined via a NLO fit [29] to LEP1 data on  $D^*$  production in  $e^+e^-$  annihilation measured by OPAL [30]. The renormalisation scale  $\mu_R$  and the factorisation scale  $\mu_F$  are in both calculations defined as  $\mu_R = \mu_F/2 = \xi m_T$  with  $m_T = \sqrt{p_T^2 + m_c^2}$  and  $\xi = 1$ , where  $p_T$  is the transverse momentum of the charm quark. The GRV [21] parametrisation of the parton distributions of the photon is used in the massless calculation and the GRS [31] parametrisation in the massive calculation. Despite the low transverse momenta studied, the agreement between data and the massless calculation is good. The massive calculation agrees with the data cross-section for  $p_T^{D^*} > 3$  GeV, but underestimates the data in the region of small  $p_T^{D^*}$ . The scale dependence on  $d\sigma/dp_T^{D^*}$  determined by using  $\xi = 1/2$  and  $\xi = 2$  is approximately 10% for both calculations. The corresponding curves for the massless case are also shown in Fig. 5. In addition, the massless calculation was performed using the AFG [32] and GS [33] parametrisations. In the massive calculation AFG and GRV were used as alternative parametrisations. The change of the cross-section is approximately 10% in both calculations.

In Table 3, the number of reconstructed  $D^*$  mesons with  $2 \text{ GeV} < p_T^{D^*} < 12 \text{ GeV}$  and  $|\eta^{D^*}| < 1.5$  and the corresponding differential cross-sections  $d\sigma/d|\eta^{D^*}|$  are given as a function of  $|\eta^{D^*}|$  for both decay modes. The numbers are determined in the same way as described above in the case of  $p_T^{D^*}$ . Within the statistical uncertainties, both decay modes yield comparable results. The combined differential cross-section is also given in Table 3 and plotted in Fig. 6. The distribution is dominated by the events at low  $p_T^{D^*}$ , and within the error, it is independent of  $|\eta^{D^*}|$ . The centres of the bins are taken as the average  $\langle |\eta^{D^*}| \rangle$  values. The massless calculation by Kniehl et al. is in good agreement with the measured differential cross-section, whereas the massive calculation of Frixione et al. underestimates the data, as seen already in Fig. 5. For the massive calculation, two additional curves are shown in Fig. 6 representing different charm quark masses  $m_c$  with renormalisation scales  $\mu_R$  and factorisation scales  $\mu_F$  as indicated in the figure. The combination of a small charm quark mass ( $m_c = 1.2$  GeV) with a special choice of the renormalisation scale ( $\mu_R = 2m_T$  for the direct and  $\mu_R = m_T/2$  for the single-resolved process) yields a cross-section which is closer to the data, but still slightly low.

For the determination of the systematic uncertainties, each decay mode and each bin in  $p_T^{D^*}$  or  $|\eta^{D^*}|$  is treated individually. The following errors are taken into account:

- The relative uncertainties on  $\text{BR}(D^{*+} \rightarrow K^- \pi^+ \pi^+)$  and  $\text{BR}(D^{*+} \rightarrow K^- \pi^+ \pi^- \pi^+ \pi^+)$  of 3.1% and 5.6%, respectively [26].
- The relative uncertainty on the selection efficiencies due to the limited number of Monte Carlo events varies between 5% in the lowest  $p_T^{D^*}$  bin for the 3-prong decay mode and 13% in the highest  $p_T^{D^*}$  bin for the 5-prong decay mode. The corresponding errors for the  $|\eta^{D^*}|$  distribution are 5% to 7% in all  $|\eta^{D^*}|$  bins except for the bin  $1 < |\eta^{D^*}| < 1.5$  in the 5-prong mode where the error is 12%.
- The uncertainty on the number of background events determined from the fit of the background function to the sum of the sidebands of the signal data and of the wrong-charge distribution. A modified background function is constructed, defined by the requirement  $\chi^2 = \chi_{\min}^2 + 1$ , where  $\chi_{\min}^2$  is the minimum  $\chi^2$  of the fit. The relative difference between the number of background events determined with the modified background function and the number of background events determined with the original background function is taken as the error. Depending on the decay mode and on the  $p_T^{D^*}$  or  $|\eta^{D^*}|$  bins, the relative uncertainties vary between 5% and 25%.
- The contributions of the direct and single-resolved Monte Carlo samples have been varied between 40% and 60%. In the 3-prong and in the 5-prong mode, the corresponding errors on the cross-sections are smaller than 7% for all bins in  $p_T^{D^*}$  and in  $|\eta^{D^*}|$ .
- Uncertainties in the modelling of the tracking in the central detector are assessed by repeating the analysis with the tracking resolutions varied in the Monte Carlo by  $\pm 10\%$  around the values that describe the data best. The efficiencies obtained are compared with the original values, and the relative difference is quoted as the systematic error. Depending on decay mode and bin, this error lies between 5% and 15%.
- Uncertainties in the  $dE/dx$  probabilities for identifying kaons. In a former OPAL analysis [34],  $D^*$  mesons are reconstructed in the 3-prong mode using a similar set of cuts to this analysis. The relative error on the  $dE/dx$  probability for identifying kaons is determined to be around 3%. In the 5-prong mode, not studied in Ref. [34], the pion tracks are also identified using the  $dE/dx$  probabilities, so the corresponding uncertainty is assumed to be 5%.

The uncertainty on the integrated luminosity  $\mathcal{L}$  is smaller than 1% and is therefore not taken into account. The individual systematic uncertainties are added quadratically, separately for each decay mode as well as for each bin in  $p_T^{D^*}$  or  $|\eta^{D^*}|$ . The integrated cross-section  $\sigma_{\text{meas}}$  of the process  $e^+e^- \rightarrow e^+e^- D^* X$  in the kinematical region  $2 \text{ GeV} < p_T^{D^*} < 12 \text{ GeV}$  and  $|\eta^{D^*}| < 1.5$  is determined to be  $\sigma_{\text{meas}}^{D^*} = 29.4 \pm 3.4(\text{stat}) \pm 2.4(\text{sys}) \text{ pb}$ .

The LO cross-sections for the direct process,  $\sigma_{\text{dir}}^{D^*}$ , and for the single-resolved process,  $\sigma_{\text{res}}^{D^*}$ , calculated with the PYTHIA Monte Carlo for different LO parametrisations of the parton densities (SaS-1D [17], GRV [21] and LAC1 [35]) are given in Table 4. In the PYTHIA Monte Carlo, the charm quark mass  $m_c$  was varied between 1.3 and 1.7 GeV. Since the ratio of direct to single-resolved cross-sections is about 1:1 in the data, the direct cross-section is well described by PYTHIA and the single-resolved cross-section is best described using GRV. The single-resolved cross-section is underestimated using SaS-1D, and the LAC1 parametrisation overestimates the single-resolved cross-section.

## 8 Total cross-section $\sigma(e^+e^- \rightarrow e^+e^-c\bar{c})$

For the determination of the total cross-section  $\sigma(e^+e^- \rightarrow e^+e^-D^*X)$ , the Monte Carlo is used to extrapolate to the full kinematical region using the relation

$$\begin{aligned}\sigma(e^+e^- \rightarrow e^+e^-D^*X) &= \sigma(e^+e^- \rightarrow e^+e^-D^*X)_{\text{dir}} + \sigma(e^+e^- \rightarrow e^+e^-D^*X)_{\text{res}} \\ &= \sigma_{\text{meas}} \left( r_{\text{dir}} \cdot \mathcal{R}_{\text{dir}}^{\text{MC}} + (1 - r_{\text{dir}}) \cdot \mathcal{R}_{\text{res}}^{\text{MC}} \right).\end{aligned}\quad (13)$$

where  $\mathcal{R}_{\text{dir}}^{\text{MC}}$  and  $\mathcal{R}_{\text{res}}^{\text{MC}}$  are the extrapolation factors. This allows the total cross-section of the process  $e^+e^- \rightarrow e^+e^-c\bar{c}$  for  $Q_i^2 < 4.5 \text{ GeV}^2$  to be calculated using the equation

$$\sigma(e^+e^- \rightarrow e^+e^-c\bar{c}) = \frac{1}{2 \cdot f(c \rightarrow D^{*+})} \cdot \sigma(e^+e^- \rightarrow e^+e^-D^*X). \quad (14)$$

In a previous publication [36], the product  $P_c = f(c \rightarrow D^{*+}) \times \text{BR}(D^{*+} \rightarrow D^0\pi^+) \times \text{BR}(D^0 \rightarrow K^-\pi^+)$  was derived from measurements of  $D^*$  production in  $e^+e^-$  collisions at  $\sqrt{s_{\text{ee}}} = 10.5$  and 30 GeV to be  $P_c = (7.1 \pm 0.5) \cdot 10^{-3}$ . With the branching ratios taken from Ref. [26], a hadronisation fraction  $f(c \rightarrow D^{*+}) = 0.270 \pm 0.019 \pm 0.010$  is derived, where the last error is due to the branching ratio uncertainties. Since the invariant mass range of the photon-photon system studied in this analysis is of the same order of magnitude as the  $e^+e^-$  energies mentioned above, this value of  $f(c \rightarrow D^*)$  is used in the analysis.

The extrapolation factors  $\mathcal{R}_{\text{dir}}^{\text{MC}}$  for the direct events and  $\mathcal{R}_{\text{res}}^{\text{MC}}$  for the single-resolved events are defined as the ratio of the number of all generated  $D^*$  mesons in the full kinematic range of  $p_{\text{T}}^{D^*}$  and  $|\eta^{D^*}|$  divided by the number of generated  $D^*$  mesons with  $2 \text{ GeV} < p_{\text{T}}^{D^*} < 12 \text{ GeV}$  and  $|\eta^{D^*}| < 1.5$ . The extrapolation factors are  $\mathcal{R}_{\text{dir}}^{\text{MC}} = 12.6$  and  $\mathcal{R}_{\text{res}}^{\text{MC}} = 18.4$  obtained using the combination  $m_c = 1.5 \text{ GeV}$  and the Peterson fragmentation with  $\epsilon_c = 0.031$ .

The extrapolation introduces systematic uncertainties due to the modelling of the fragmentation of the charm quarks into  $D^*$  mesons which influence mainly the  $p_{\text{T}}^{D^*}$  distributions. To determine the systematic errors on the extrapolation factors, different  $m_c$  values and different fragmentation functions were used for the event generation in the Monte Carlo:

- The charm quark mass  $m_c$  was varied between 1.3 and 1.7 GeV.
- $\epsilon_c = 0.0851$  [29] was used in the Peterson fragmentation function.
- The Lund symmetric fragmentation function [37] was used with the parameters  $a = 1.95$  and  $b = 1.58$  determined in Ref. [36].
- In case of the single-resolved process, the GRV parametrisation was used as an alternative parametrisation in combination with different charm quark masses and fragmentation functions.

For all studied combinations of  $m_c$ , fragmentation functions and parametrisations of the parton densities, the direct and the single-resolved Monte Carlo samples were added in such a way that in the kinematical range  $2 \text{ GeV} < p_{\text{T}}^{D^*} < 12 \text{ GeV}$  and  $|\eta^{D^*}| < 1.5$  the cross-section

is equal to  $\sigma_{\text{meas}}$ , the direct contribution is  $r_{\text{dir}} = 51\%$  and the single-resolved contribution is  $1 - r_{\text{dir}} = 49\%$ . The resulting differential cross-sections  $d\sigma/dp_T^{D^*}$  and  $d\sigma/d|\eta^{D^*}|$  are in agreement with the measured differential cross-sections (Figs. 5-6). Therefore the mean quadratic deviation of all calculated extrapolation factors from the central values  $\mathcal{R}_{\text{dir}}^{\text{MC}} = 12.6$  and  $\mathcal{R}_{\text{res}}^{\text{MC}} = 18.4$  is used to determine the relative systematic uncertainties of 19% for  $\mathcal{R}_{\text{dir}}^{\text{MC}}$  and 27% for  $\mathcal{R}_{\text{res}}^{\text{MC}}$ .

Combining Eqs. (13) and (14), we determine the total cross-section of the process  $e^+e^- \rightarrow e^+e^-c\bar{c}$  to be  $\sigma(e^+e^- \rightarrow e^+e^-c\bar{c}) = 842 \pm 97 \text{ (stat)} \pm 75 \text{ (sys)} \pm 196 \text{ (extr) pb}$  at  $\sqrt{s_{\text{ee}}} = 183 - 189 \text{ GeV}$ . The first error is the statistical, the second error is the systematic error and the third error is the extrapolation uncertainty. The direct contribution is determined to be  $\sigma(e^+e^- \rightarrow e^+e^-c\bar{c})_{\text{dir}} = 351 \pm 40 \text{ (stat)} \pm 79 \text{ (sys)} \pm 66 \text{ (extr) pb}$  and the single-resolved contribution to be  $\sigma(e^+e^- \rightarrow e^+e^-c\bar{c})_{\text{res}} = 491 \pm 56 \text{ (stat)} \pm 111 \text{ (sys)} \pm 130 \text{ (extr) pb}$ .

The separation of direct and resolved events in heavy quark production is scheme-dependent in the NLO massless calculation, but it is unambiguous in LO and in the NLO massive calculation. Using  $m_c = 1.5 \text{ GeV}$ , the LO direct cross-section in PYTHIA lies in the range  $300_{-44}^{+41} \text{ pb}$ . The LO calculation of Ref. [2] gives  $382_{-94}^{+186} \text{ pb}$ , and the NLO calculation  $593_{-198}^{+319} \text{ pb}$ . The upper and lower error correspond to  $m_c = 1.3$  and  $1.7 \text{ GeV}$ , respectively. The OPAL anti-tagging condition was applied to these calculations. The measured direct cross-section agrees well with the LO calculations, whereas it lies at the lower end of the NLO calculation. This could be due to the separation procedure for direct and single-resolved events which uses distributions from a LO Monte Carlo.

Fig. 7 shows the total cross-section  $\sigma(e^+e^- \rightarrow e^+e^-c\bar{c})$  compared to other measurements and to the NLO calculation of Ref. [2] using the GRS parton distributions. The calculation is in good agreement with the OPAL result within the large band of uncertainties due to variations of  $m_c$ ,  $\mu_R$  and  $\mu_F$ . The anti-tagging condition used in this paper has been applied to the NLO calculation. It should be noted that the anti-tagging conditions of the different experiments are not identical. The OPAL result is consistent with the L3 result at  $\sqrt{s_{\text{ee}}} = 167 \text{ GeV}$  and about 1.5 standard deviations below the L3 result at  $\sqrt{s_{\text{ee}}} = 183 \text{ GeV}$  [39].

## 9 Determination of $F_{2,c}^\gamma$

In this section, deep inelastic electron-photon scattering is studied using single-tagged events. The  $D^*$  production cross-section, as well as the charm production cross-section and the charm structure function  $F_{2,c}^\gamma$  of the photon are determined from events with a beam electron scattered into the forward detectors (tagged events). An event is tagged (SW-tagged or FD-tagged) if the energy of the scattered electron  $E'$ , measured in the angular range  $33 \text{ mrad} < \theta' < 55 \text{ mrad}$  for the SW or  $60 \text{ mrad} < \theta' < 120 \text{ mrad}$  for the FD, exceeds  $50 \text{ GeV}$  in one hemisphere of the detector. The corresponding approximate ranges in  $Q^2$  are  $5 \text{ GeV}^2 < Q^2 < 30 \text{ GeV}^2$  and  $30 \text{ GeV}^2 < Q^2 < 100 \text{ GeV}^2$  for SW-tagged and FD-tagged events, respectively. The selection of  $D^*$  candidates is identical to the selection in the anti-tagged case, with three exceptions:

- For the calculation of the visible invariant mass  $W_{\text{vis}}$ , clusters in the SW or FD in the hemisphere of the tag are excluded.



- The combinatorial background in tagged events is smaller due to the slightly smaller mean number of tracks per event. This makes it possible to include  $D^*$  mesons with  $p_T^{D^*} > 1$  GeV for SW-tagged events.
- In FD-tagged events, the  $D^*$  mesons have higher transverse momenta  $p_T^{D^*}$  due to the transverse momentum balance between the tagged electron and the hadronic system. To improve the signal to background ratio, a cut  $p_T^{D^*} > 3$  GeV is applied for FD-tagged events.

Fig. 1 shows the distribution of the difference between the  $D^*$  and the  $D^0$  candidate mass found in the tagged sample. The fit of the background function Eq. 9 to the upper sideband of the signal was performed in the range  $154.5 \text{ MeV} < \Delta M < 200.5 \text{ MeV}$ . The  $\chi^2$  of the fit result is 25 for 21 degrees of freedom. Subtracting the background predicted by the fit,  $29.8 \pm 5.9$  (stat)  $D^*$  mesons are found in the signal region of the tagged events. The combinatorial background in the upper sideband is also well described by the tagged wrong-charge sample. Background subtraction with the wrong-charge sample gives a consistent result for the number of  $D^*$  events. Due to the small number of  $D^*$  mesons both  $D^*$  decay modes are combined for the further analysis. No double-tagged  $D^*$  event has been found, i.e. an event with energy deposits of more than 50 GeV in the forward calorimeters in both hemispheres.

Fig. 8 shows the distributions of  $W_{\text{vis}}$  and of the measured  $Q^2$  of the tagged signal events, and the  $p_T^{D^*}$  distribution is presented in Fig. 9. The data are compared to the predictions of the HERWIG and Vermaseren Monte Carlo generators, normalised to the number of data events. Both Monte Carlo generators give a good description of the shape of the data distributions.

We determine the cross-section for  $D^*$  production in deep inelastic electron-photon scattering in the well-measured kinematic range:  $p_T^{D^*} > 1$  GeV for an electron scattering angle  $33 \text{ mrad} < \theta' < 55 \text{ mrad}$  (SW) or  $p_T^{D^*} > 3$  GeV for  $60 \text{ mrad} < \theta' < 120 \text{ mrad}$  (FD),  $|\eta^{D^*}| < 1.5$  and  $E' > 50 \text{ GeV}$ ,  $5 \text{ GeV}^2 < Q^2 < 100 \text{ GeV}^2$ ; using almost the whole accessible  $Q^2$  range defined by  $\theta'$  and  $E'$ .

The analysis is performed in two bins of  $x$  with  $0.0014 < x < 0.1$  and  $0.1 < x < 0.87$ . The  $x$  range is limited by the  $Q^2$  range, by the minimum kinematically allowed invariant mass  $W > 3.88 \text{ GeV}$  needed to produce a  $D^*$  meson, and by the event selection cut  $W_{\text{vis}} < 60 \text{ GeV}$ . To take into account the detector acceptance and resolution in  $x$  the data are corrected using a  $2 \times 2$  matrix. The measured  $x_{\text{vis}}$  is calculated from Eq. 6 using  $W_{\text{vis}}$  and the measured value of  $Q^2$ . The resolution effects in the  $Q^2$  reconstruction are small compared to the resolution effects in measuring  $x$ . They can therefore be neglected.

The  $D^*$  selection efficiency for  $x > 0.1$  is given by the ratio of the number of reconstructed  $D^*$  mesons originating from events with  $x > 0.1$  to all generated  $D^*$  mesons in events with  $x > 0.1$ , in the restricted kinematic range defined above. The selection efficiency for  $x > 0.1$  is about  $(21 \pm 2)\%$  (not including the branching ratios). For  $x > 0.1$  the selection efficiencies obtained from both Monte Carlo generators are consistent, but for  $x < 0.1$  the selection efficiencies are around  $(30 \pm 3)\%$  according to HERWIG and around  $(18 \pm 2)\%$  according to Vermaseren. Both programs predict that about one third of the selected  $D^*$  events generated with  $x < 0.1$  are reconstructed with  $x_{\text{vis}} > 0.1$ , whereas migration from  $x > 0.1$  to  $x_{\text{vis}} < 0.1$  is very small.

Table 5 summarises the number of reconstructed  $D^*$  mesons and gives the measured values of the cross-section

$$\sigma_{\text{tag}}^{D^*} = \frac{N_{D^*}^{\text{cor}}}{\text{BR} \cdot \mathcal{L}}, \quad (15)$$

which is the deep inelastic electron-photon scattering cross-section for  $D^*$  production in the restricted kinematic range as defined above. It is calculated from the number of  $D^*$  events,  $N_{D^*}^{\text{cor}}$ , obtained from the  $2 \times 2$  matrix correction using both HERWIG and Vermaseren. For the combined  $D^*$  branching ratios into the 3-prong and 5-prong mode, we use  $\text{BR} = 0.0782 \pm 0.0030$  [26]. The total integrated luminosity  $\mathcal{L}$  is  $220 \text{ pb}^{-1}$ . The average of the cross-sections corrected with HERWIG and Vermaseren is also given in Table 5.

For  $x > 0.1$ , both Monte Carlo models yield consistent results. For  $x < 0.1$ , the difference between the cross-sections  $\sigma_{\text{tag}}^{D^*}$  obtained using HERWIG and Vermaseren is due to the different  $D^*$  selection efficiencies. The following systematic errors on  $\sigma_{\text{tag}}^{D^*}$  are taken into account:

- The limited number of Monte Carlo events leads to an uncertainty of approximately 15% on  $\sigma_{\text{tag}}^{D^*}$  for each of the Monte Carlo generators.
- Within the statistical uncertainties, the HERWIG and Vermaseren models yield consistent corrected numbers of  $D^*$  mesons for  $x > 0.1$ , whereas for  $x < 0.1$ , the corrected numbers of  $D^*$  mesons obtained with the HERWIG and Vermaseren Monte Carlo models differ by more than 2 standard deviations. Therefore only for  $x < 0.1$ , half the difference between  $\sigma_{\text{tag}}^{D^*}$  using HERWIG and Vermaseren is taken as error on the averaged value of  $\sigma_{\text{tag}}^{D^*}$ .
- The combined relative uncertainty on the branching ratios  $\text{BR}(D^{*+} \rightarrow K^- \pi^+ \pi^+)$  and  $\text{BR}(D^{*+} \rightarrow K^- \pi^+ \pi^- \pi^+ \pi^+)$  is 3.8% [26].
- The uncertainty in the number of background events in the signal region estimated in the same way as for anti-tagged events gives relative errors of 12% for  $x < 0.1$  and 6% for  $x > 0.1$ .
- The relative uncertainty due to the modelling of the tracking in the central detector is estimated to be 8% using the corresponding errors determined for the differential cross-sections  $d\sigma/dp_T^{D^*}$  and  $d\sigma/d|\eta^{D^*}|$  for the anti-tagged events.
- The relative uncertainty due to the use of the  $dE/dx$  probabilities for identifying kaons and pions is estimated to be 4%, also using the corresponding errors determined for the differential cross-sections  $d\sigma/dp_T^{D^*}$  and  $d\sigma/d|\eta^{D^*}|$  for the anti-tagged events.
- The uncertainty due to the measurement of the energy  $E'$  of the tagged electron is assessed by shifting the reconstructed quantity in the Monte Carlo according to its resolution and by repeating the analysis. The change on  $\sigma_{\text{tag}}^{D^*}$  is around 3% and is taken into account as relative error. The uncertainty due to the measurement of the scattering angle  $\theta'$  is determined in the same way as for  $E'$ . The relative change on  $\sigma_{\text{tag}}^{D^*}$  is found to be only around 1%. This error is therefore neglected. The uncertainty due to the measurement of the visible invariant mass  $W_{\text{vis}}$  of the event is estimated to be only around 1% and is therefore also neglected.

All systematic errors are added in quadrature.

For the determination of the total cross-section of  $D^*$  production in deep inelastic electron-photon scattering,  $\sigma(e^+e^- \rightarrow e^+e^-D^*X)$ , the Monte Carlo models are used to extrapolate to the whole kinematic region. This allows the total charm cross-section in deep inelastic electron-photon scattering to be calculated via the relation

$$\begin{aligned}\sigma(e^+e^- \rightarrow e^+e^-c\bar{c}) &= \frac{1}{2 \cdot f(c \rightarrow D^{*+})} \cdot \sigma(e^+e^- \rightarrow e^+e^-D^*X) \\ &= \frac{1}{2 \cdot f(c \rightarrow D^{*+})} \cdot \mathcal{R}_{\text{tag}}^{\text{MC}} \cdot \sigma_{\text{tag}}^{D^*}.\end{aligned}\tag{16}$$

The extrapolation factor  $\mathcal{R}_{\text{tag}}^{\text{MC}}$  is defined in the same way as in the anti-tagged case. Table 6 gives the values of the total charm cross-section,  $\sigma(e^+e^- \rightarrow e^+e^-c\bar{c})$ , extrapolated using HERWIG and Vermaseren as well as the averaged cross-section. The extrapolation error has been determined in the following way:

For  $x > 0.1$ , both Monte Carlo generators predict very similar values for  $\mathcal{R}_{\text{tag}}^{\text{MC}}$  (4.8/4.6 for HERWIG/Vermaseren) and thus for  $\sigma(e^+e^- \rightarrow e^+e^-c\bar{c})$ . The uncertainty on  $\mathcal{R}_{\text{tag}}^{\text{MC}}$  is determined in the same way as in the anti-tagged case. It is found that the influence of the charm quark mass and fragmentation function is small, and the relative uncertainty on  $\mathcal{R}_{\text{tag}}^{\text{MC}}$  and thus on the averaged cross-section  $\sigma(e^+e^- \rightarrow e^+e^-c\bar{c})$  is only 5%.

In contrast, for  $x < 0.1$ , the Monte Carlo generators predict very different extrapolation factors due to the large discrepancy between the predicted invisible part of the cross-section. For  $x < 0.1$ , the HERWIG extrapolation factor,  $\mathcal{R}_{\text{tag}}^{\text{MC}} = 12.9$ , is more than twice as large as the Vermaseren factor  $\mathcal{R}_{\text{tag}}^{\text{MC}} = 5.1$ . The predicted cross-sections of the Monte Carlo models and the NLO calculation of Laenen et al. [4] are given in Table 7. Since the hadron-like contribution is neglected in the QPM, the Vermaseren cross-section is much smaller than the LO and the NLO cross-section for  $x < 0.1$ . In contrast, mainly due to the massless approach taken, the prediction from HERWIG is higher than the cross-section from the LO and the NLO calculation. Therefore it is likely that the correct cross-section, and therefore the correct extrapolation factor, lies within the range of the two Monte Carlo predictions. Half the difference between the two extrapolated cross-sections is taken into account as extrapolation error on the averaged cross-section  $\sigma(e^+e^- \rightarrow e^+e^-c\bar{c})$ .

Finally, the value of the charm structure function  $F_{2,c}^\gamma(x, \langle Q^2 \rangle)$  of the photon, averaged over the corresponding bin in  $x$ , is determined by

$$F_{2,c}^\gamma(x, \langle Q^2 \rangle) = \sigma(e^+e^- \rightarrow e^+e^-c\bar{c}) \cdot \left( \frac{F_{2,c}^\gamma(x, \langle Q^2 \rangle)}{\sigma(e^+e^- \rightarrow e^+e^-c\bar{c})} \right)_{\text{NLO}},\tag{17}$$

where the ratio  $(F_{2,c}^\gamma(x, \langle Q^2 \rangle)/\sigma(e^+e^- \rightarrow e^+e^-c\bar{c}))_{\text{NLO}}$  is given by the NLO calculation of Laenen et al. [4]. The mean virtuality in the measured region  $5 \text{ GeV}^2 < Q^2 < 100 \text{ GeV}^2$  is about  $\langle Q^2 \rangle \approx 20 \text{ GeV}^2$ , in agreement with the values from the generated HERWIG and Vermaseren Monte Carlo events. The  $F_{2,c}^\gamma(x, \langle Q^2 \rangle)$  values are given in Table 6. They are calculated from the individual charm cross-sections obtained using the HERWIG and Vermaseren models and from the averaged cross-section.

In Fig. 10 a), the measured cross-sections obtained using the individual Monte Carlo models, are compared to the calculation of Laenen et al. [4] performed in LO and NLO and to the Monte Carlo results, and Fig. 10 b) shows the charm structure function  $F_{2,c}^\gamma$ . The NLO prediction is based on  $m_c = 1.5$  GeV and the renormalisation and factorisation scales are chosen to be  $\mu_R = \mu_F = Q$ . The calculation is obtained for the sum of the point-like and hadron-like contributions to  $F_{2,c}^\gamma$ , using the GRV-NLO parametrisation in the calculation of the hadron-like part. The NLO corrections are predicted to be small for the whole  $x$  range. The NLO calculation is shown as a band representing the uncertainty of the theoretical prediction, evaluated by varying the charm quark mass between 1.3 and 1.7 GeV and by changing the renormalisation and factorisation scales in the range  $Q/2 \leq \mu_R = \mu_F \leq 2 Q$ .

For  $x > 0.1$ , all cross-section predictions in Fig. 10 a) are consistent with one another. Because the cross-section prediction from the Vermaseren model is consistent with the point-like contribution to the LO calculation for the whole  $x$  range, the contributions from longitudinal photons are expected to be small. For  $x < 0.1$ , the situation is different. The NLO calculation predicts the hadron-like and point-like component to be of about equal size. Therefore the purely point-like QPM prediction of the Vermaseren model is expected to underestimate the data if a hadron-like contribution exists. The HERWIG Monte Carlo predicts the highest cross-section, which is expected, since the massless approach should overestimate the cross-section, as explained in Section 4.

The different behaviour of the Monte Carlo cross-sections in the two regions of  $x$  is reflected in the measured cross-sections shown in Fig. 10 a). For  $x > 0.1$  the individual measured cross-sections obtained by correcting with HERWIG and Vermaseren are very similar, the error of the measured cross-section is dominated by the statistical uncertainty, and the NLO calculation is in good agreement with the data. In contrast, for  $x < 0.1$ , the result suffers from the strong model dependence discussed above. The result based on the HERWIG generator is much higher than the result obtained using the Vermaseren model. Despite this uncertainty the corrected data suggest a cross-section which is above the purely point-like component, i.e. the hadron-like component of  $F_{2,c}^\gamma$  is non-zero. This observation is independent of the Monte Carlo model chosen for correction. Averaging the individual results is therefore safe for  $x > 0.1$ , but for  $x < 0.1$  the averaged result suffers from large model uncertainties and has to be interpreted with care. In Fig. 10 b) the cross-section measurements are converted into the measured charm structure function using Eq. 17. The conclusions derived from  $F_{2,c}^\gamma$  and from the cross-sections are the same.

In Fig. 11, the averaged results are presented. Fig. 11 a) shows the cross-section on a linear scale in  $x$  in comparison to the same predictions as in Fig. 10. In Fig. 11 b) the charm structure function is presented on a logarithmic scale in  $x$  for  $\langle Q^2 \rangle = 20 \text{ GeV}^2$ . The data points for  $F_{2,c}^\gamma$  are located at the mean value of  $x$ , denoted with  $\langle x \rangle$ . The values are the averaged  $\langle x \rangle$  values obtained with both Monte Carlo generators, and half the difference of the HERWIG and Vermaseren predictions is taken as the uncertainty. For  $x > 0.1$ , the predicted  $\langle x \rangle$  is around 0.32 and the difference between the HERWIG and Vermaseren programs is invisible. The point-like contribution decreases for decreasing  $x$ , whereas the hadron-like component rises. Consequently, for  $x < 0.1$ , the HERWIG Monte Carlo predicts a smaller average value of  $\langle x \rangle = 0.028$  than the Vermaseren Monte Carlo which yields  $\langle x \rangle = 0.054$ .

In addition to the full NLO prediction, the predicted hadron-like component of  $F_{2,c}^\gamma$  is also shown in Fig. 11 b). This contribution is very small for  $x > 0.1$  and therefore in this range the NLO calculation is an almost purely perturbative prediction with the charm quark mass and the strong coupling constant as the only free parameters. This prediction nicely describes the data. To illustrate the shape of  $F_{2,c}^\gamma$  the data are also compared to the GRS-LO [31] prediction and to the point-like component alone both shown for  $Q^2 = 20 \text{ GeV}^2$ . The point-like component strongly decreases for decreasing  $x$ . The full  $F_{2,c}^\gamma$  evaluated at  $Q^2 = 20 \text{ GeV}^2$  agrees with the data. The change of  $F_{2,c}^\gamma$  within the range of  $Q^2$  studied is large. The maximum value of  $F_{2,c}^\gamma$  for  $x > 0.1$  rises by about a factor of five between  $Q^2 = 5 \text{ GeV}^2$  and  $Q^2 = 100 \text{ GeV}^2$  and the charm thresholds moves from about  $x = 0.35$  to about  $x = 0.9$ .

In conclusion, for  $x > 0.1$ , the purely perturbative NLO calculation is in good agreement with the measurement and for  $x < 0.1$ , the measurement suffers from large uncertainties of the invisible cross-section predicted by the HERWIG and Vermaseren Monte Carlo models, and therefore the result is not very precise. However, despite the large error in this region the data suggest a non-zero hadron-like component of  $F_{2,c}^\gamma$ .

## 10 Conclusion

We have measured the inclusive production of  $D^{*\pm}$  mesons in photon-photon collisions using the OPAL detector at LEP at  $e^+e^-$  centre-of-mass energies  $\sqrt{s_{ee}} = 183$  and  $189 \text{ GeV}$ . The  $D^{*+}$  mesons are reconstructed in their decay to  $D^0\pi^+$  with the  $D^0$  observed in the two decay modes  $K^-\pi^+$  and  $K^-\pi^+\pi^-\pi^+$ . In total,  $100.4 \pm 12.6$  (stat)  $D^*$  mesons are selected in anti-tagged events and  $29.8 \pm 5.9$  (stat)  $D^*$  mesons in single-tagged events.

In the anti-tagged event sample, the direct and single-resolved contributions are separated using di-jet events reconstructed with a cone jet finding algorithm, and for all observed events by fitting the distribution of the scaled  $D^*$  transverse momentum  $x_T^{D^*}$ . Both methods yield consistent results, and due to the larger statistics used, the second method is more precise. It is found that in the kinematical region  $p_T^{D^*} > 2 \text{ GeV}$  and  $|\eta^{D^*}| < 1.5$  the direct contribution to the process  $e^+e^- \rightarrow e^+e^-D^*X$  is  $(51 \pm 10)\%$  and that the single-resolved contribution is  $(49 \pm 10)\%$ .

Differential cross-sections as functions of the  $D^*$  transverse momentum and pseudorapidity are measured for anti-tagged events and are compared to a NLO calculation by Kniehl et al. [29] using the massless approach, and by Frixione et al. [3] using the massive approach. It is found that despite the low values of  $p_T^{D^*}$  studied the massless calculation is in good agreement with the data. The massive calculation agrees with the measured cross-section for  $p_T^{D^*} > 3 \text{ GeV}$  but underestimates the data for lower values of  $p_T^{D^*}$ .

The total cross-section of the process  $e^+e^- \rightarrow e^+e^-c\bar{c}$ , where the charm quarks are produced in the collision of two quasi-real photons, is measured to be  $\sigma(e^+e^- \rightarrow e^+e^-c\bar{c}) = 842 \pm 97$  (stat)  $\pm 75$  (sys)  $\pm 196$  (extr) pb, with a direct contribution of  $\sigma(e^+e^- \rightarrow e^+e^-c\bar{c})_{\text{dir}} = 351 \pm 40$  (stat)  $\pm 79$  (sys)  $\pm 66$  (extr) pb and a single-resolved contribution of  $\sigma(e^+e^- \rightarrow e^+e^-c\bar{c})_{\text{res}} = 491 \pm 56$  (stat)  $\pm 111$  (sys)  $\pm 130$  (extr) pb. The NLO calculation of Ref. [2] and the measurements by L3 [39] are in agreement with this result.

The first measurement of the charm structure function  $F_{2,c}^\gamma(x, \langle Q^2 \rangle)$  of the photon has been performed based on  $29.8 \pm 5.9$  (stat)  $D^*$  mesons reconstructed in single-tagged events. The value of  $F_{2,c}^\gamma(x, \langle Q^2 \rangle)$  is determined for an average  $\langle Q^2 \rangle$  of 20 GeV<sup>2</sup> and in two regions of  $x$ ,  $0.0014 < x < 0.1$  and  $0.1 < x < 0.87$ . The NLO corrections to  $F_{2,c}^\gamma(x, \langle Q^2 \rangle)$  are predicted to be small for all  $x$  and the contribution of the hadron-like component is negligible for  $x > 0.1$ , which means that  $F_{2,c}^\gamma(x, \langle Q^2 \rangle)$  can be predicted purely perturbatively in this region. For  $x > 0.1$ , the perturbative NLO calculation of Laenen et al. [4] is in good agreement with the measurement. For  $x < 0.1$ , the measurement suffers from large uncertainties of the invisible cross-section predicted by the HERWIG and Vermaseren Monte Carlo models, and therefore the result is not very precise. However, despite the large error in this region the data suggest a non-zero hadron-like component of  $F_{2,c}^\gamma$ .

## Acknowledgements

We especially wish to thank Michael Krämer and Eric Laenen for many interesting and valuable discussions and good collaboration. We are grateful to them, to Stefano Frixione and to Bernd Kniehl for providing their NLO calculations.

We particularly wish to thank the SL Division for the efficient operation of the LEP accelerator at all energies and for their continuing close cooperation with our experimental group. We thank our colleagues from CEA, DAPNIA/SPP, CE-Saclay for their efforts over the years on the time-of-flight and trigger systems which we continue to use. In addition to the support staff at our own institutions we are pleased to acknowledge the

Department of Energy, USA,

National Science Foundation, USA,

Particle Physics and Astronomy Research Council, UK,

Natural Sciences and Engineering Research Council, Canada,

Israel Science Foundation, administered by the Israel Academy of Science and Humanities,

Minerva Gesellschaft,

Benozziyo Center for High Energy Physics,

Japanese Ministry of Education, Science and Culture (the Monbusho) and a grant under the Monbusho International Science Research Program,

Japanese Society for the Promotion of Science (JSPS),

German Israeli Bi-national Science Foundation (GIF),

Bundesministerium für Bildung, Wissenschaft, Forschung und Technologie, Germany,

National Research Council of Canada,

Research Corporation, USA,

Hungarian Foundation for Scientific Research, OTKA T-029328, T023793 and OTKA F-023259.

## References

- [1] M. Cacciari, M. Greco, B.A. Kniehl, M. Krämer, G. Kramer and M. Spira, Nucl. Phys. B466 (1996) 173.
- [2] M. Drees, M. Krämer, J. Zunft and P.M. Zerwas, Phys. Lett. B306 (1993) 371; M. Krämer, private communications.
- [3] S. Frixione, M. Krämer and E. Laenen, *D\* Production in Two-Photon Collisions*, hep-ph/9908483, submitted to Nucl. Phys. (1999).
- [4] E. Laenen, S. Riemersma, J. Smith and W.L. van Neerven, Phys. Rev. D49 (1994) 5753; E. Laenen and S. Riemersma, Phys. Lett. B376 (1996) 169.
- [5] JADE Collaboration, W. Bartel et al., Phys. Lett. B184 (1987) 288.
- [6] TASSO Collaboration, W. Braunschweig et al., Z. Phys. C47 (1990) 499.
- [7] TPC/2 $\gamma$  Collaboration, M. Alston-Garnjost et al., Phys. Lett. B252 (1990) 499.
- [8] TOPAZ Collaboration, R. Enomoto et al., Phys. Lett. B328 (1994) 535; R. Enomoto et al., Phys. Rev. D50 (1994) 1879.
- [9] AMY Collaboration, N. Takashimizu et al., Phys. Lett. B381 (1996) 372.
- [10] ALEPH Collaboration, D. Buskulic et al., Phys. Lett. B355 (1995) 595.
- [11] L3 Collaboration, M. Acciarri et al., *Measurement of Inclusive D $^{*\pm}$  Production in Two-Photon Collisions*, CERN-EP/99-106, accepted by Phys. Lett. B (1999).
- [12] OPAL Collaboration, K. Ahmet et al., Nucl. Instr. and Methods A305 (1991) 275; P.P. Allport et al., Nucl. Instr. and Methods A346 (1994) 476; P.P. Allport et al., Nucl. Instr. and Methods A324 (1993) 34; O. Biebel et al., Nucl. Instr. and Methods A323 (1992) 169; M. Hauschild et al., Nucl. Instr. and Methods A314 (1992) 74.
- [13] B.E. Anderson et al., IEEE Trans. Nucl. Sci. 41 (1994) 845.
- [14] P. Kessler, Il Nuovo Cimento 17 (1960) 809.
- [15] C. Berger and W. Wagner, Phys. Rep. 146 (1987) 1.
- [16] T. Sjöstrand, Comp. Phys. Comm. 82 (1994) 74.
- [17] G.A. Schuler and T. Sjöstrand, Z. Phys. C68 (1995) 607.
- [18] C. Peterson, D. Schlatter, I. Schmitt and P.M. Zerwas, Phys. Rev. D27 (1983) 105.
- [19] G. Marchesini et al., Comp. Phys. Comm. 67 (1992) 465.
- [20] J. Smith, J.A.M. Vermaseren and G. Grammer Jr., Phys. Rev. D15 (1977) 3280; J.A.M. Vermaseren, J. Smith and G. Grammer Jr., Phys. Rev. D19 (1979) 137; J.A.M. Vermaseren, Nucl. Phys. B229 (1983) 347; R. Bhattacharya, G. Grammer Jr. and J. Smith, Phys. Rev. D15 (1977) 3267.

- [21] M. Glück, E. Reya and A. Vogt, Phys. Rev. D46 (1992) 1973;  
M. Glück, E. Reya and A. Vogt, Phys. Rev. D45 (1992) 3986.
- [22] J. Fujimoto et al., Comp. Phys. Comm. 100 (1997) 128.
- [23] J. Allison et al., Nucl. Instr. and Methods. A317 (1992) 47.
- [24] OPAL Collaboration, G. Alexander et al., Phys. Lett. B377 (1996) 181.
- [25] OPAL Collaboration, G. Alexander et al., Phys. Lett. B262 (1991) 341;  
OPAL Collaboration, R. Akers et al., Z. Phys. C60 (1993) 601.
- [26] C. Caso et al., Review of Particle Physics, Euro. Phys. J. C3 (1998) 1.
- [27] OPAL Collaboration, G. Abbiendi et al., *Di-Jet Production in Photon-Photon Collisions at  $\sqrt{s_{ee}} = 161$  and  $172$  GeV*, CERN-EP/98-113, accepted by Euro. Phys. J. C (1999).
- [28] G.D. Lafferty and T.R. Wyatt, Nucl. Instr. and Methods A355 (1995) 541.
- [29] J. Binnewies, B.A. Kniehl and G. Kramer, Phys. Rev. D58 (1998) 014014;  
J. Binnewies, B.A. Kniehl and G. Kramer, Phys. Rev. D53 (1996) 6110.
- [30] OPAL Collaboration, K. Ackerstaff et al., Euro. Phys. J. C1 (1998) 439.
- [31] M. Glück, E. Reya and I. Schienbein, Phys. Rev. D60 (1999) 054019.
- [32] P. Aurenche, J.P. Guillet and M. Fontannaz, Z. Phys. C64 (1994) 621.
- [33] L.E. Gordon and J.K. Storrow, Nucl. Phys. B489 (1997) 405.
- [34] OPAL Collaboration, G. Abbiendi et. al., *Measurement of the Production Rate of Charm Quark Pairs from Gluons in Hadronic  $Z^0$  Decays*, CERN-EP/99-089, accepted by Euro. Phys. J. C. (1999).
- [35] H. Abramowicz, K. Charchula and A. Levy, Phys. Lett. B269 (1991) 458.
- [36] OPAL Collaboration, R. Akers et al., Z. Phys. C67 (1995) 27.
- [37] B. Andersson, G. Gustafson and B. Söderberg, Z. Phys. C20 (1983) 317;  
M.G. Bowler, Z. Phys. C11 (1981) 169;  
D.A. Morris, Nucl. Phys. B313 (1989) 634.
- [38] G. Altarelli, T. Sjöstrand and F. Zwirner, *Physics at LEP2*, CERN 96-01 (1996).
- [39] L3 Collaboration, M. Acciarri et al., Phys. Lett. B453 (1999) 83.



	$D^0 \rightarrow K^- \pi^+$	$D^0 \rightarrow K^- \pi^+ \pi^- \pi^+$
direct	$(40.8 \pm 1.7)\%$	$(14.4 \pm 0.8)\%$
single-resolved	$(38.1 \pm 2.0)\%$	$(11.2 \pm 0.9)\%$

Table 1:  $D^*$  selection efficiencies  $\epsilon$  for the two decay modes and for direct and single-resolved events as determined from the PYTHIA Monte Carlo (for anti-tagged events only). The selection efficiencies refer to  $D^*$  mesons with  $p_T^{D^*} > 2$  GeV and  $|\eta^{D^*}| < 1.5$ . Only statistical errors are given.

$p_T^{D^*}$ [GeV]	$\langle p_T^{D^*} \rangle$ [GeV]	$N_{D^*}^{\text{rec}}$		$d\sigma/dp_T^{D^*}$ [pb/GeV]		
		$K^- \pi^+$	$K^- \pi^+ \pi^- \pi^+$	$K^- \pi^+$	$K^- \pi^+ \pi^- \pi^+$	combined
2 – 3	2.46	$42.9 \pm 7.7$	$27.4 \pm 7.3$	$20.6 \pm 3.7 \pm 3.0$	$21.5 \pm 5.8 \pm 6.1$	$20.8 \pm 3.1 \pm 2.4$
3 – 5	3.82	$18.4 \pm 4.5$	$11.4 \pm 4.2$	$3.7 \pm 0.9 \pm 0.5$	$3.1 \pm 1.2 \pm 0.7$	$3.5 \pm 0.7 \pm 0.3$
5 – 12	7.30	$8.3 \pm 3.0$	$4.5 \pm 2.2$	$0.38 \pm 0.14 \pm 0.06$	$0.25 \pm 0.12 \pm 0.05$	$0.31 \pm 0.09 \pm 0.09$

Table 2: Number of reconstructed  $D^*$  mesons with  $|\eta^{D^*}| < 1.5$  in bins of  $p_T^{D^*}$  for both decay modes after background subtraction (for anti-tagged events only). The differential  $D^*$  cross-section as a function of  $p_T^{D^*}$  for each decay mode and the combined cross-section is also given. The first error is statistical and the second error is systematic.

$ \eta^{D^*} $	$N_{D^*}^{\text{rec}}$		$d\sigma/d \eta^{D^*} $ [pb]		
	$K^-\pi^+$	$K^-\pi^+\pi^-\pi^+$	$K^-\pi^+$	$K^-\pi^+\pi^-\pi^+$	combined
0.0 – 0.5	$29.1 \pm 5.9$	$17.0 \pm 5.3$	$22.6 \pm 4.6 \pm 2.7$	$18.0 \pm 5.6 \pm 4.7$	$21.0 \pm 3.5 \pm 2.1$
0.5 – 1.0	$18.1 \pm 5.3$	$24.0 \pm 5.8$	$14.5 \pm 4.2 \pm 3.8$	$23.8 \pm 5.8 \pm 4.9$	$18.0 \pm 3.4 \pm 2.8$
1.0 – 1.5	$22.8 \pm 5.0$	$6.3 \pm 3.7$	$25.3 \pm 5.6 \pm 2.9$	$19.5 \pm 11.7 \pm 6.1$	$24.2 \pm 5.0 \pm 2.2$

Table 3: Number of reconstructed  $D^*$  mesons with  $2 \text{ GeV} < p_T^{D^*} < 12 \text{ GeV}$  in bins of  $|\eta^{D^*}|$  for both decay modes after background subtraction (for anti-tagged events only). The differential  $D^*$  cross-section as a function of  $|\eta^{D^*}|$  for each decay mode and the combined cross-section is also given. The first error is statistical and the second error is systematic.

	$\sigma_{\text{dir}}^{D^*}$ [pb]	$\sigma_{\text{res}}^{D^*}$ [pb]		
PYTHIA	14.0 - 14.9	3.8 - 5.5 (SaS-1D)	6.9 - 9.9 (GRV)	23.0 - 37.0 (LAC1)

Table 4: Predicted integrated LO cross-section of the process  $e^+e^- \rightarrow e^+e^-D^*X$  in the kinematical region  $2 \text{ GeV} < p_T^{D^*} < 12 \text{ GeV}$  and  $|\eta^{D^*}| < 1.5$  calculated with the PYTHIA Monte Carlo using different parametrisations of the parton densities (anti-tagged events only). Direct and single-resolved cross-sections are given separately. The charm quark mass was varied between 1.3 and 1.7 GeV.

$x$	$N_{D^*}^{\text{rec}}$	$\sigma_{\text{tag}}^{D^*}$ [pb], corrected with		$\sigma_{\text{tag}}^{D^*}$ [pb]
		HERWIG	Vermaseren	average
0.0014 – 0.1	$9.9 \pm 3.6$	$3.1 \pm 1.1 \pm 0.7$	$4.7 \pm 1.8 \pm 0.9$	$3.9 \pm 1.4 \pm 1.0$
0.1 – 0.87	$20.0 \pm 4.7$	$4.0 \pm 1.4 \pm 0.7$	$4.0 \pm 1.4 \pm 0.7$	$4.0 \pm 1.4 \pm 0.6$

Table 5: Number of reconstructed  $D^*$  mesons,  $N_{D^*}^{\text{rec}}$ , found in tagged events and  $\sigma_{\text{tag}}^{D^*}$ , obtained by correcting with HERWIG and Vermaseren in two bins of  $x$ , where  $\sigma_{\text{tag}}^{D^*}$  is the deep inelastic electron-photon scattering cross-section for  $D^*$  production in the restricted kinematic range as defined in the text. The first error on  $\sigma_{\text{tag}}^{D^*}$  is the statistical error of the data and the second error is the systematic error. The right hand column gives the averaged cross-sections obtained by correcting with the two Monte Carlo models.

$x$	$\sigma(e^+e^- \rightarrow e^+e^-c\bar{c})$ [pb], corrected with		$\sigma(e^+e^- \rightarrow e^+e^-c\bar{c})$ [pb]
	HERWIG	Vermaseren	average
0.0014 – 0.1	$92.6 \pm 34.1 \pm 24.6$	$36.9 \pm 13.6 \pm 9.8$	$64.8 \pm 23.9 \pm 17.2 \pm 27.9$
0.1 – 0.87	$35.5 \pm 12.4 \pm 5.2$	$34.3 \pm 11.9 \pm 5.1$	$34.9 \pm 12.1 \pm 5.1 \pm 1.7$
$x$	$F_{2,c}^\gamma(x, \langle Q^2 \rangle)/\alpha$ , corrected with		$F_{2,c}^\gamma(x, \langle Q^2 \rangle)/\alpha$
	HERWIG	Vermaseren	average
0.0014 – 0.1	$0.39 \pm 0.14 \pm 0.10$	$0.16 \pm 0.06 \pm 0.04$	$0.27 \pm 0.10 \pm 0.07 \pm 0.12$
0.1 – 0.87	$0.11 \pm 0.04 \pm 0.02$	$0.11 \pm 0.04 \pm 0.02$	$0.11 \pm 0.04 \pm 0.02 \pm 0.01$

Table 6: Total charm cross-section in deep inelastic electron-photon scattering,  $\sigma(e^+e^- \rightarrow e^+e^-c\bar{c})$ , for  $5 \text{ GeV}^2 < Q^2 < 100 \text{ GeV}^2$  and the charm structure function of the photon divided by the fine structure constant,  $F_{2,c}^\gamma(x, \langle Q^2 \rangle)/\alpha$ , averaged over the corresponding bin in  $x$  for  $\langle Q^2 \rangle = 20 \text{ GeV}^2$ . The cross-section and  $F_{2,c}^\gamma(x, \langle Q^2 \rangle)/\alpha$  are presented corrected using both the HERWIG and Vermaseren Monte Carlo models. The averaged values for the cross-section and  $F_{2,c}^\gamma(x, \langle Q^2 \rangle)/\alpha$  are also given. The first errors are statistical, the second errors systematic, and the third errors are the extrapolation uncertainties.

$x$	$\sigma(e^+e^- \rightarrow e^+e^-c\bar{c})$ [pb]				$F_{2,c}^\gamma(x, \langle Q^2 \rangle)/\alpha$	
	HERWIG	Vermaseren	LO	NLO	LO	NLO
0.0014 – 0.1	22.6	7.7	15.3	$16.3^{+2.8}_{-2.1}$	0.070	$0.069^{+0.043}_{-0.024}$
0.1 – 0.87	20.3	24.7	26.1	$30.1^{+6.9}_{-5.5}$	0.082	$0.097^{+0.024}_{-0.019}$

Table 7: Predicted total charm cross-section in deep inelastic electron-photon scattering,  $\sigma(e^+e^- \rightarrow e^+e^-c\bar{c})$ , for  $5 \text{ GeV}^2 < Q^2 < 100 \text{ GeV}^2$  according to the Monte Carlo generators HERWIG and Vermaseren and according to the calculation of Laenen et al. [4] performed in LO and NLO. For the calculation, also the  $F_{2,c}^\gamma(x, \langle Q^2 \rangle)/\alpha$  prediction is quoted in LO and NLO for  $Q^2 = 20 \text{ GeV}^2$ . The errors of the NLO results are obtained by varying the charm quark mass and the renormalisation and factorisation scales in the calculation.

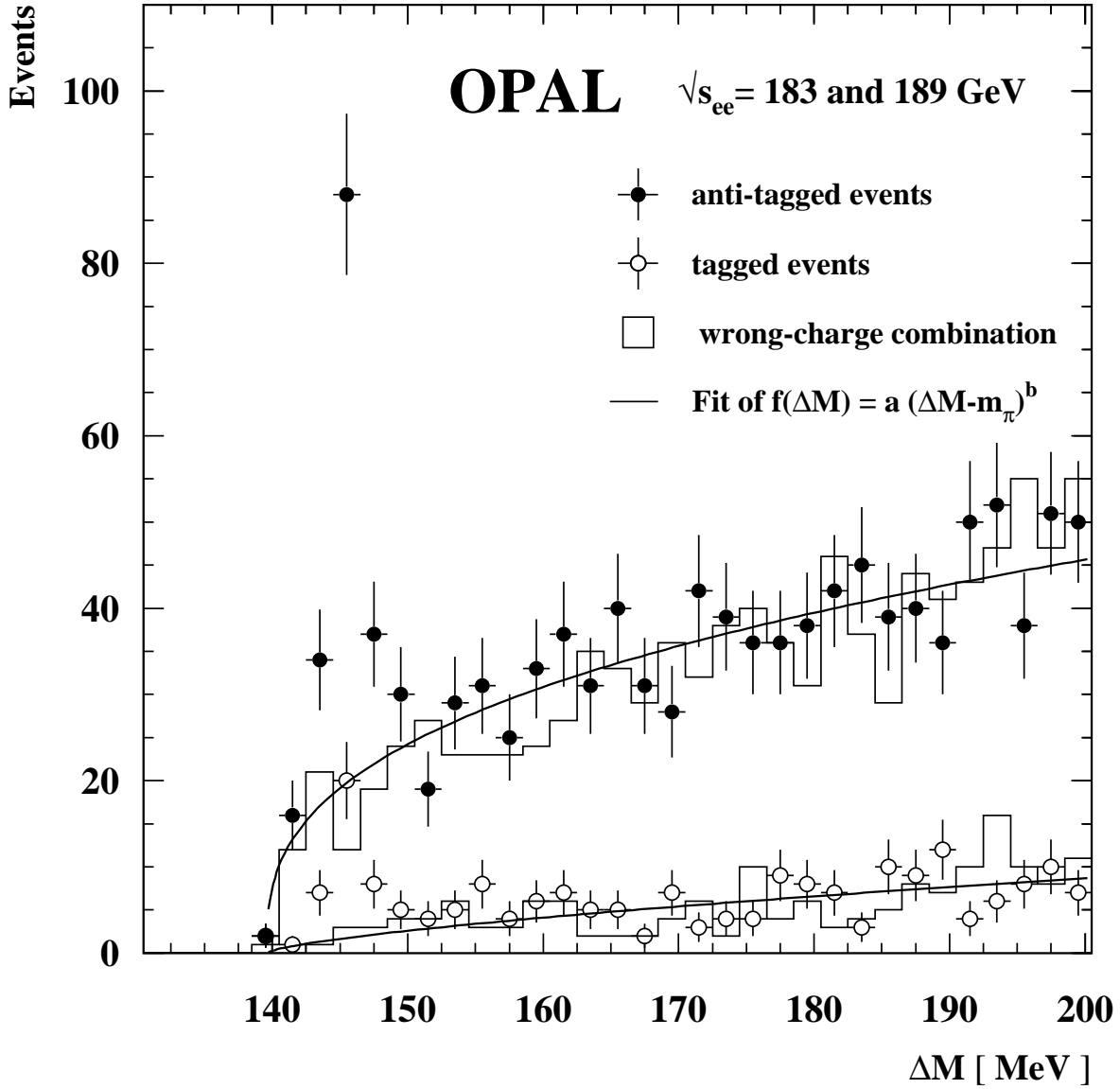


Figure 1: Mass difference  $\Delta M \equiv M_{D^*}^{\text{cand}} - M_{D^0}^{\text{cand}}$  for both decay modes for the anti-tagged and tagged sample. In both samples, a clear peak is visible around  $\Delta M \equiv M_{D^*} - M_{D^0} = 145.4 \text{ MeV}$ . The result of a fit of the background function  $f(\Delta M) = a \cdot (\Delta M - m_\pi)^b$  to the upper sidebands is superimposed. The fit regions are  $\Delta M > 160.5 \text{ MeV}$  for the anti-tagged events and  $\Delta M > 154.5 \text{ MeV}$  for the tagged events. The open histograms represent the corresponding wrong-charge background samples which give a good description of the combinatorial background.

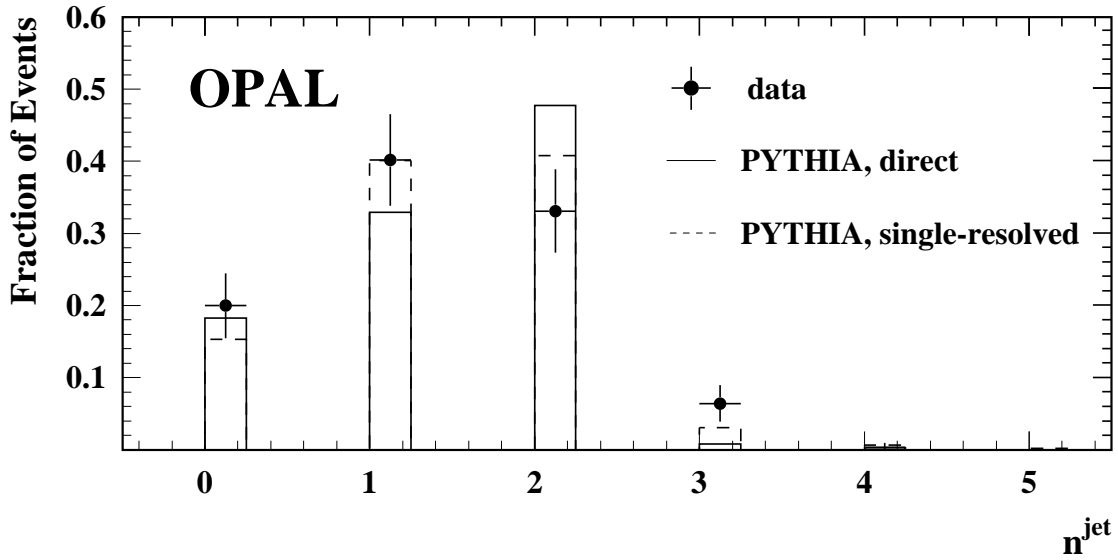


Figure 2: Fraction of signal events with different  $n^{\text{jet}}$  determined with the cone jet finding algorithm (for anti-tagged events). The dots represent the data after subtraction of the combinatorial background. The solid line shows the PYTHIA prediction for the direct and the dashed line for the single-resolved sample, respectively.

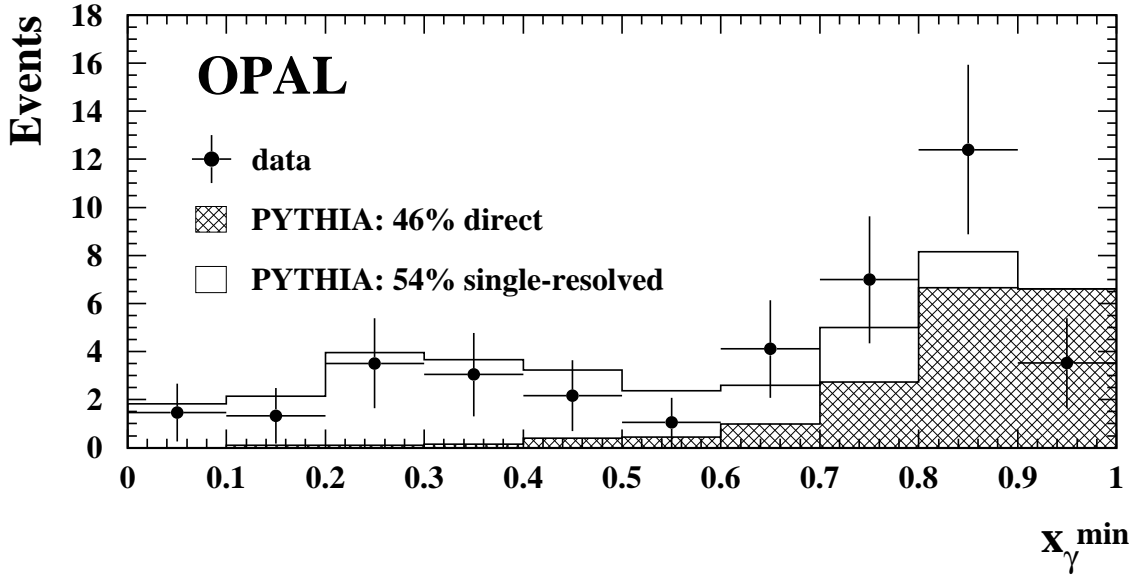


Figure 3: Minimum of  $x_\gamma^+$  or  $x_\gamma^-$  for di-jet events in the signal region (anti-tagged events only). The data, represented by the dots, are background subtracted using sideband events. The enhancement at large values of  $x_\gamma^{\text{min}}$  is due to the direct process. The histograms are the result of a fit of the relative contributions of the direct and single-resolved Monte Carlo samples to the data. The open histogram shows the single-resolved, the hatched histogram the direct contribution to the fit result.

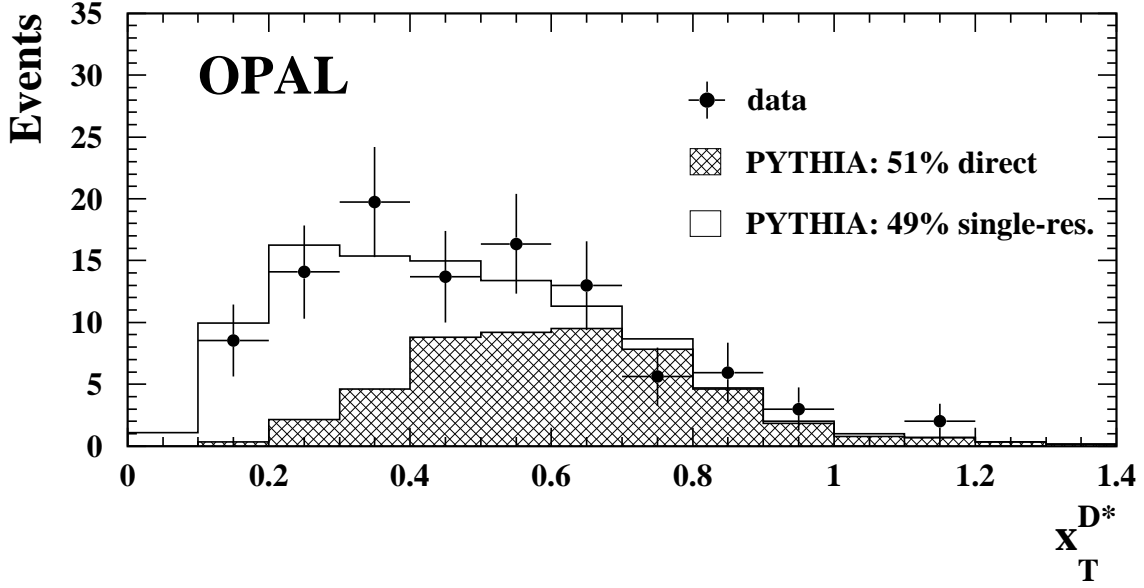


Figure 4: Scaled transverse momentum of the  $D^*$  meson,  $x_T^{D*}$ , for all signal events (anti-tagged events only). The dots represent the background subtracted data. The histograms are the result of a fit of the relative contributions of the direct and single-resolved Monte Carlo samples to the data. The open histogram shows the single-resolved, the hatched histogram the direct contribution to the fit result.

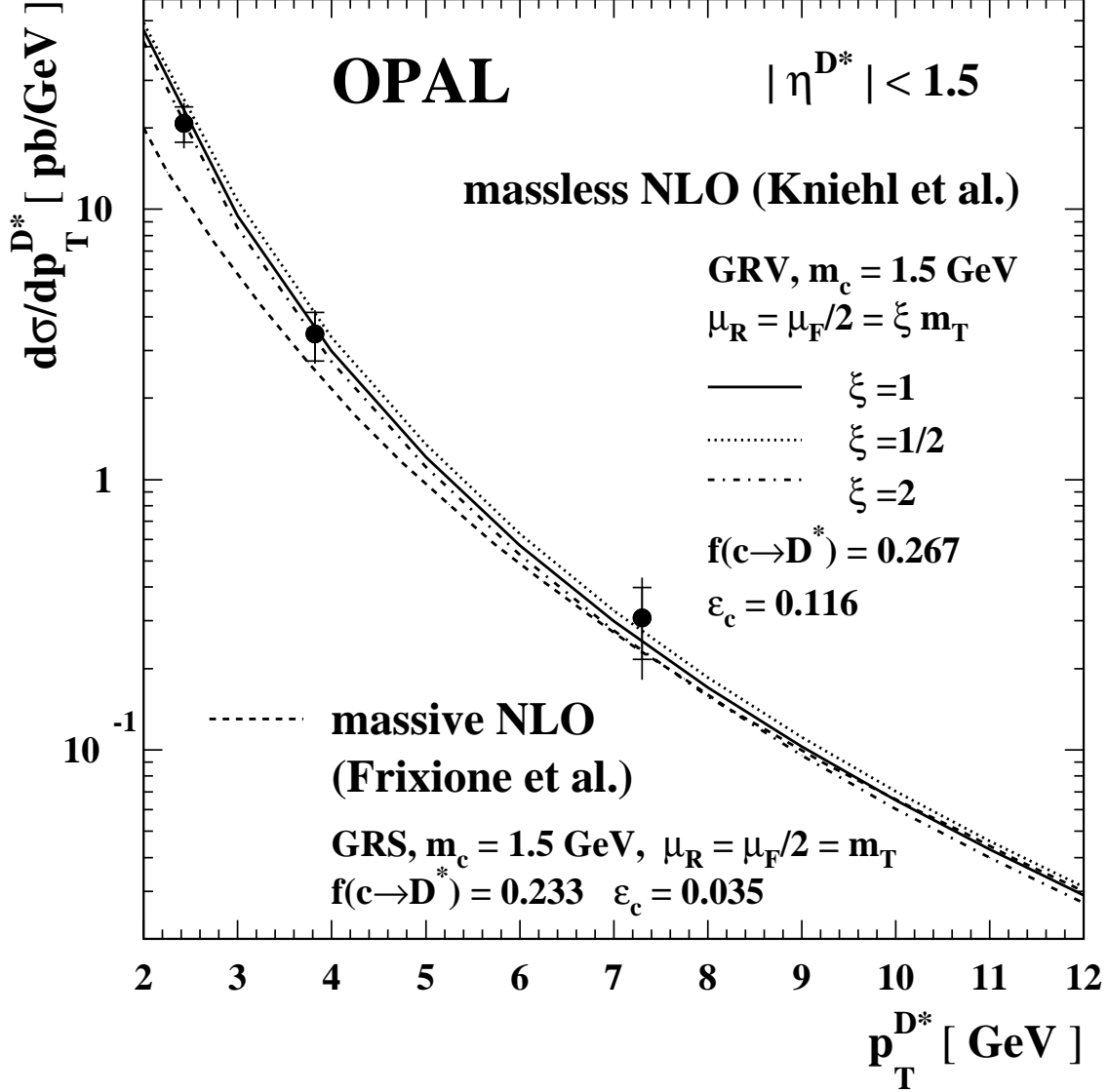


Figure 5: The differential  $D^*$  cross-section,  $d\sigma/dp_T^{D^*}$ , for the process  $e^+e^- \rightarrow e^+e^-D^*X$  in the range  $|\eta^{D^*}| < 1.5$  (for anti-tagged events). The dots represent the combined cross-sections from both decay modes. The inner error bars give the statistical error and the outer error bars the statistical and the systematic error added in quadrature. The data are compared to a NLO calculation by Kniehl et al. using the massless approach for three different renormalisation and factorisation scales,  $\mu_R$  and  $\mu_F$ , and to a NLO calculation by Frixione et al. using the massive approach. The quantity  $m_T$  is defined as  $m_T = \sqrt{p_T^2 + m_c^2}$  where  $p_T$  is the transverse momentum of the charm quark.

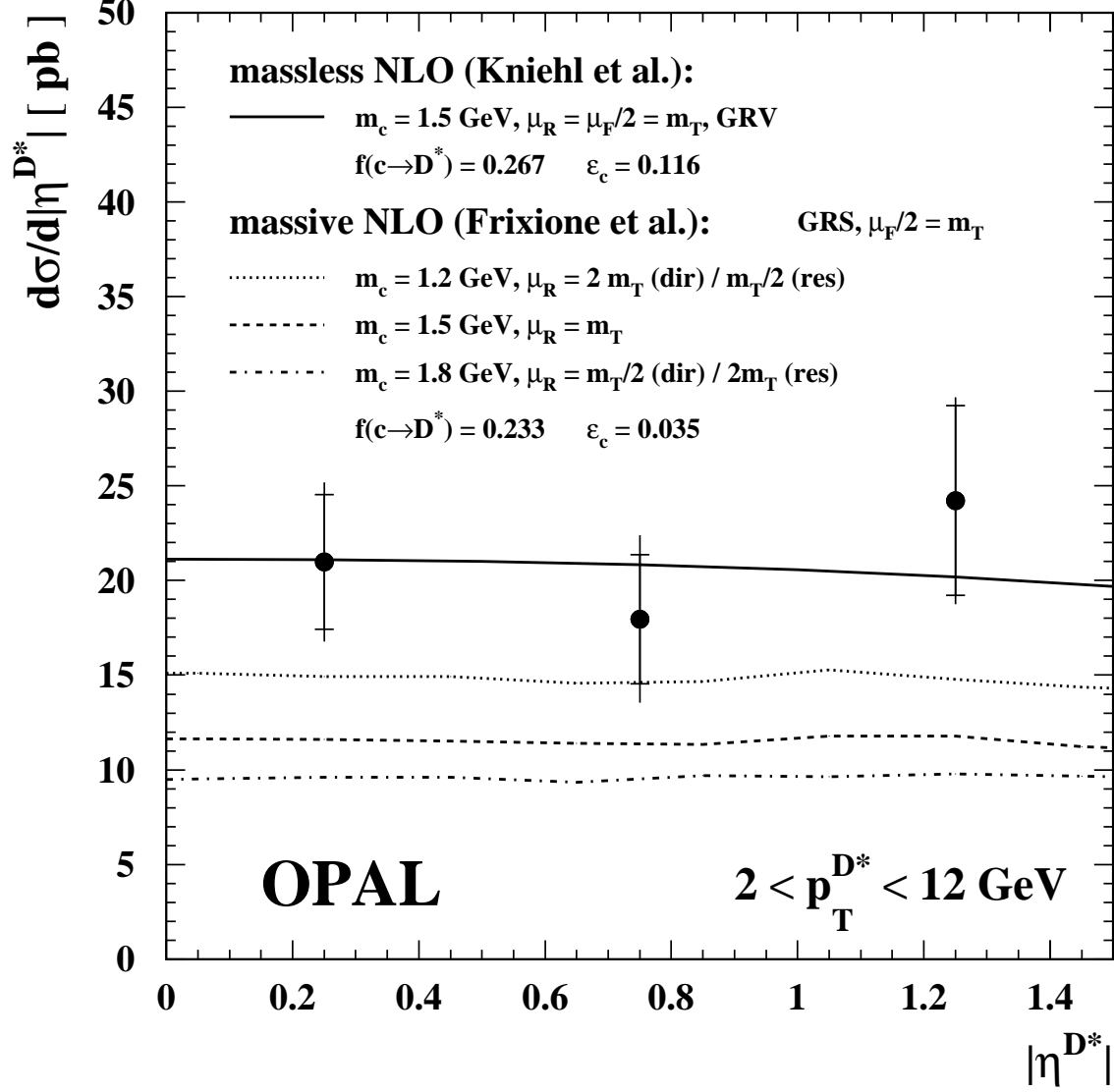


Figure 6: The differential  $D^*$  cross-section  $d\sigma/d|\eta^{D*}|$  for the process  $e^+e^- \rightarrow e^+e^-D^*X$  in the range  $2 \text{ GeV} < p_T^{D*} < 12 \text{ GeV}$  (for anti-tagged events). The dots represent the combined cross-sections from both investigated decay modes. The inner error bars give the statistical error and the outer error bars the statistical and the systematic error added in quadrature. NLO QCD calculations by Kniesl et al. using the massless approach are also shown as well as NLO QCD calculations by Frixione et al. using the massive approach using different renormalisation scales separately for the direct (dir) and the single-resolved (res) contributions and different charm quark masses. The quantity  $m_T$  is defined as  $m_T = \sqrt{p_T^2 + m_c^2}$ , where  $p_T$  is the transverse momentum of the charm quark.



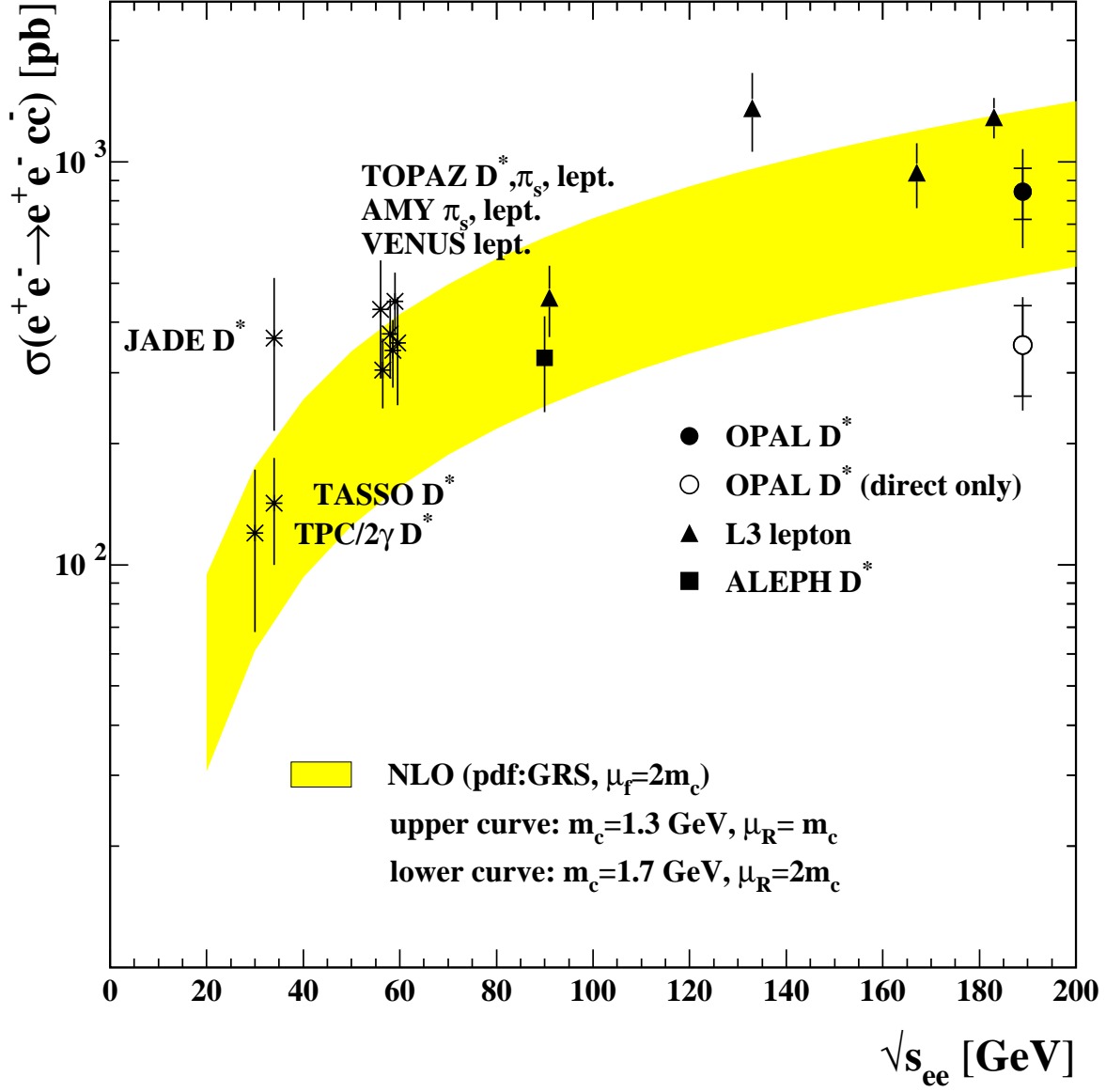


Figure 7: Comparison of measured cross-sections for the process  $e^+e^- \rightarrow e^+e^-c\bar{c}$  where the charm quarks are produced in the collision of two quasi-real photons. The outer error bars on the OPAL points represent the total errors, including the extrapolation uncertainty, and the inner bars are the statistical errors. The values for TASSO, TPC/ $2\gamma$ , JADE, TOPAZ, AMY and VENUS are taken from Ref. [38], for ALEPH from Ref. [10] and for L3 from Ref. [39]. The band shows a NLO calculation of the process  $e^+e^- \rightarrow e^+e^-c\bar{c}$  [2] for a charm quark mass between 1.3 and 1.7 GeV using the GRS parametrisation for the parton distributions of the photon.

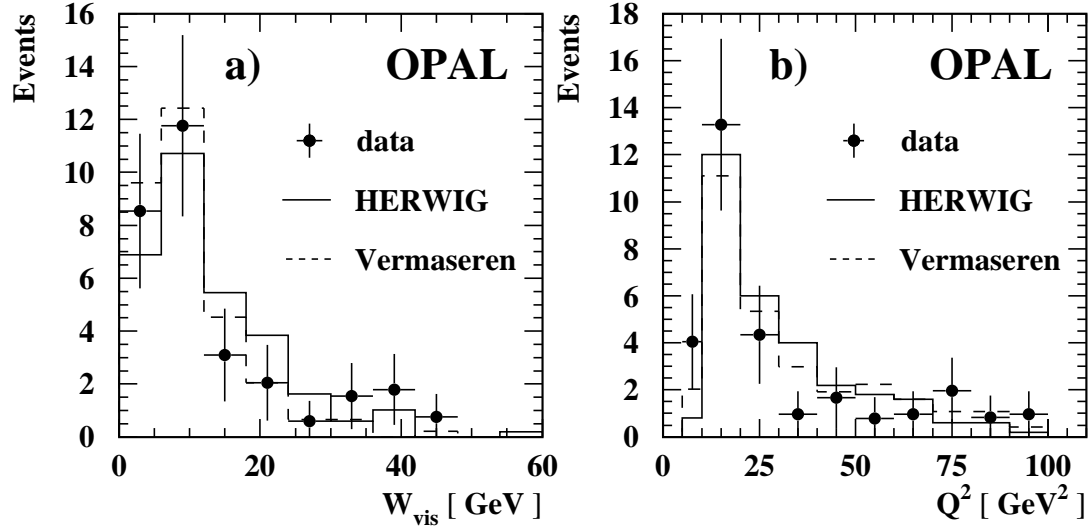


Figure 8: The distributions of a) the visible invariant mass,  $W_{\text{vis}}$ , and b) the negative four-momentum squared,  $Q^2$ , for the tagged signal events. The data are compared to the predictions of the HERWIG and Vermaseren generators. The Monte Carlo distributions are normalised to the number of data events.

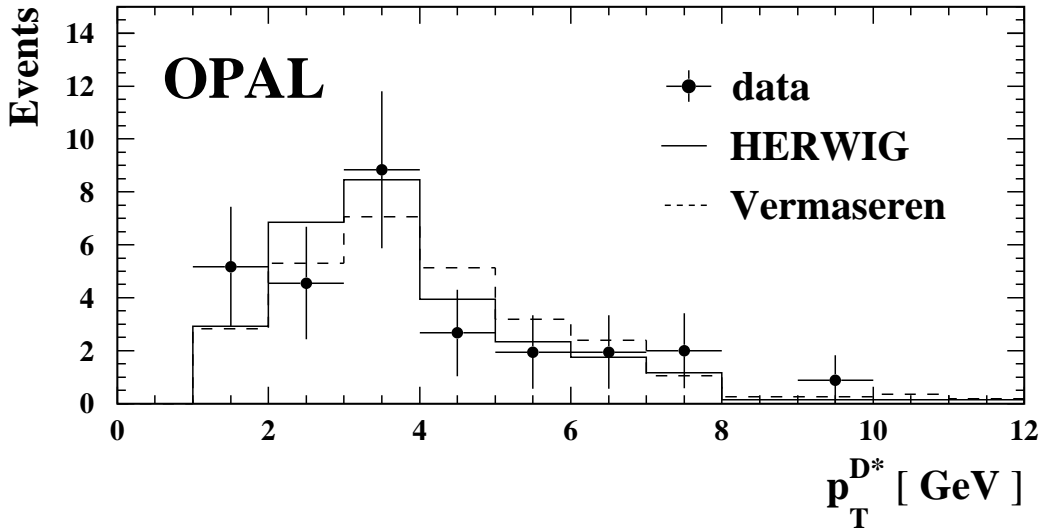


Figure 9: The distribution of transverse momentum  $p_T^{D^*}$  for the  $D^*$  mesons in the tagged signal events. The data are compared to the predictions of the HERWIG and Vermaseren generators. The Monte Carlo distributions are normalised to the number of data events.

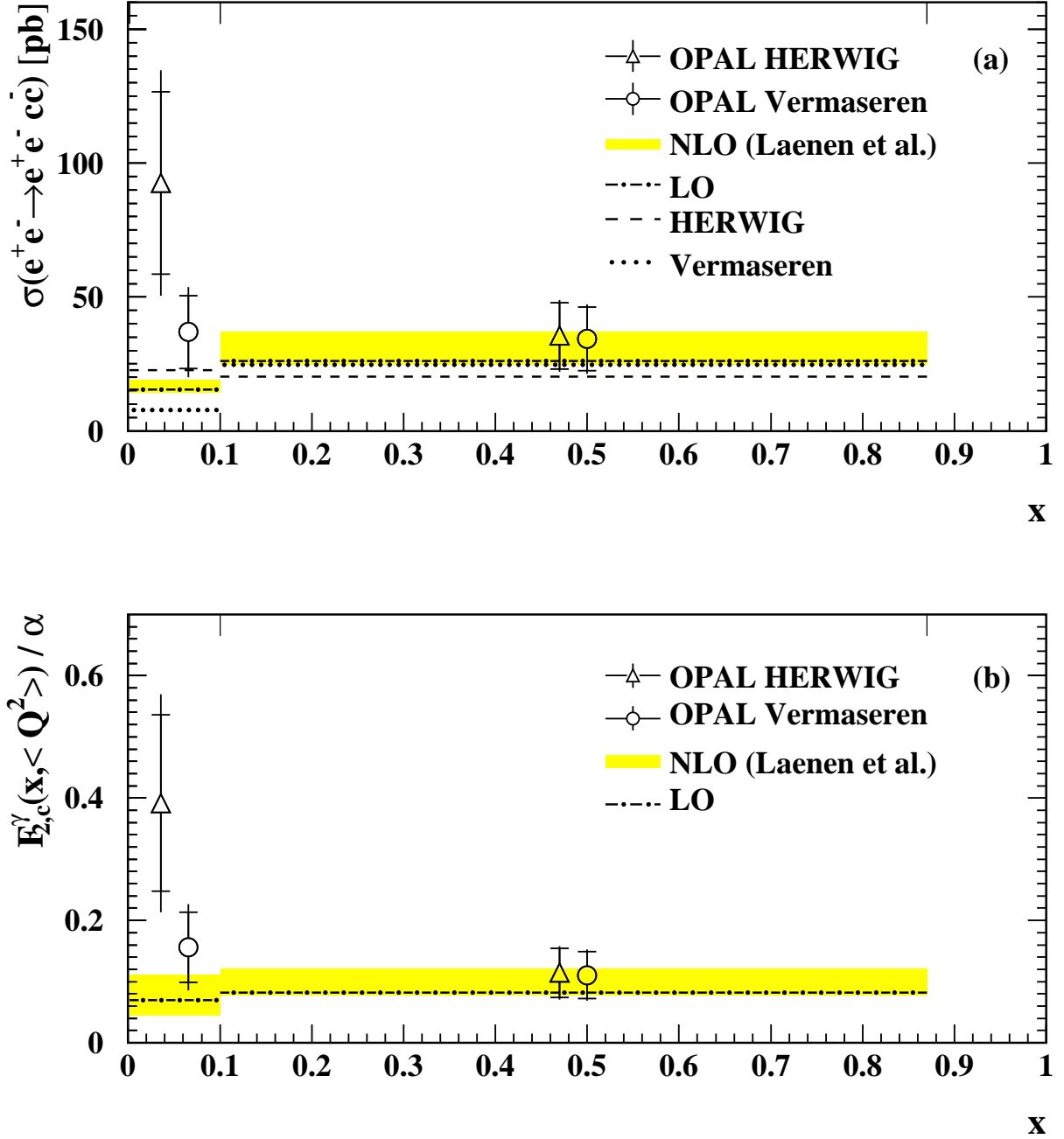


Figure 10: Results compared with predictions for a) the deep inelastic electron-photon scattering cross-section  $\sigma(e^+e^- \rightarrow e^+e^- c\bar{c})$ , with  $5 \text{ GeV}^2 < Q^2 < 100 \text{ GeV}^2$  and b) for the charm structure function of the photon divided by the fine structure constant,  $F_{2,c}^\gamma(x, \langle Q^2 \rangle) / \alpha$  at  $\langle Q^2 \rangle = 20 \text{ GeV}^2$ . The data are shown individually corrected with the HERWIG and Vermaseren Monte Carlo generators. The inner error bar is the statistical and the outer error bar is the full error. The measurements are presented at the central  $x$  values of the bins. The results obtained with the HERWIG and Vermaseren generators are slightly separated for a better visibility. The calculation of Laenen et al. [4] is performed in LO and NLO. The band for the NLO calculation indicates the theoretical uncertainties assessed by varying the charm quark mass and renormalisation and factorisation scales.

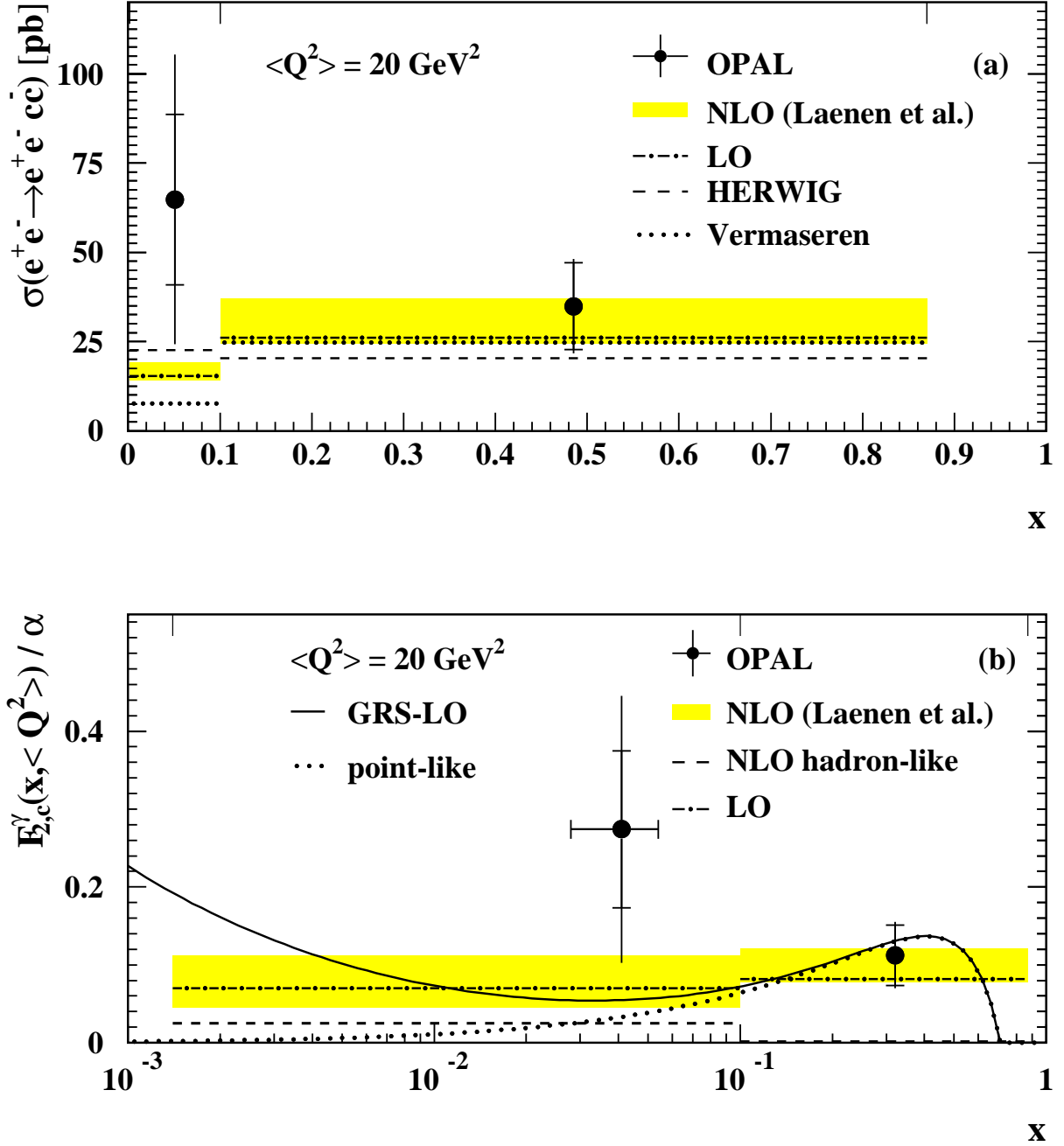


Figure 11: OPAL results for a) the deep inelastic electron-photon scattering cross-section  $\sigma(e^+e^- \rightarrow e^+e^-c\bar{c})$ , with  $5 \text{ GeV}^2 < Q^2 < 100 \text{ GeV}^2$  and b) for the charm structure function of the photon divided by the fine structure constant,  $F_{2,c}^\gamma(x, \langle Q^2 \rangle) / \alpha$ , for an average  $\langle Q^2 \rangle$  of  $20 \text{ GeV}^2$ . The data points are obtained averaging the results obtained with the HERWIG and Vermaseren Monte Carlo models. The outer error bar is the total error and the inner error bar the statistical error. The  $x$  values of the data points are obtained by averaging the mean  $x$  values taken from the HERWIG and Vermaseren generators. The data are compared to the calculation of Laenen et al. [4] performed in LO and NLO. The band for the NLO calculation indicates the theoretical uncertainties assessed by varying the charm quark mass and renormalisation and factorisation scales. In a) the cross-section predictions of the Monte Carlo generators HERWIG and Vermaseren are also given. b) also shows the prediction of the GRS-LO parametrisation for the whole structure function at  $\langle Q^2 \rangle = 20 \text{ GeV}^2$  and the point-like component alone.